Observations of Water Frost on Mars With THEMIS: Application to the Presence of Brines and the Stability of (Sub)Surface Water Ice

L Lange, S Piqueux, C S Edwards, F Forget, Joseph Naar, E Vos, A Szantai

JGR Planets

RESEARCH ARTICLE

10.1029/2024JE008489

Observations of Water Frost on Mars With THEMIS: Application to the Presence of Brines and the Stability of (Sub)Surface Water Ice

L. Lange[1], S. Piqueux[2], C. S. Edwards[3], F. Forget[1], J. Naar[4], E. Vos[1], and A. Szantai[1]

[1]Laboratoire de Météorologie Dynamique, Institut Pierre-Simon Laplace (LMD/IPSL), Sorbonne Université, Centre National de la Recherche Scientifique (CNRS), École Polytechnique, École Normale Supérieure (ENS), Paris, France, [2]Jet Propulsion Laboratory, California Institute of Technology, Pasadena, CA, USA, [3]Department of Astronomy and Planetary Science, Northern Arizona University, Flagstaff, AZ, USA, [4]Laboratoire Atmosphères, Milieux, Observations Spatiales (LATMOS/CNRS), Paris, France

Key Points:

- Seasonal water frosts on Mars are identified with coincident visible and temperature data obtained with THEMIS poleward of 48°N and 21°S
- Water frosts remain too cold to melt as pure ice. However, the warmest frost deposits observed may co-exist with brines
- Warm water frost, which releases a large amount of water vapor when it sublimates, cannot stabilize the low-latitude subsurface ice

Correspondence to:

L. Lange,
lucas.lange@lmd.ipsl.fr

Citation:

Lange, L., Piqueux, S., Edwards, C. S., Forget, F., Naar, J., Vos, E., & Szantai, A. (2024). Observations of water frost on Mars with THEMIS: Application to the presence of brines and the stability of (sub)surface water ice. *Journal of Geophysical Research: Planets*, *129*, e2024JE008489. https://doi.org/10.1029/2024JE008489

Received 7 MAY 2024
Accepted 26 AUG 2024

Abstract Characterizing the exchange of water between the Martian atmosphere and the (sub)surface is a major challenge for understanding the mechanisms that regulate the water cycle. Here we present a new data set of water ice detected on the Martian surface with the Thermal Emission Imaging System (THEMIS). The detection is based on the correlation between bright blue-white patterns in visible images and a temperature measured in the infrared that is too warm to be associated with CO_2 ice and interpreted instead as water ice. Using this method, we detect ice down to 21.4°S, 48.4°N, on pole-facing slopes at mid-latitudes, and on any surface orientation poleward of 45° latitude. Water ice observed with THEMIS is most likely seasonal rather than diurnal. Our data set is consistent with near-infrared frost detections and predictions by the Mars Planetary Climate Model. Water frost average temperature is 170 K, and the maximum temperature measured is 243 K, lower than the water ice melting point. Melting of pure water ice on the surface is unlikely due to cooling by latent heat during its sublimation. However, 243 THEMIS images show frosts that are hot enough to form brines if salts are present on the surface. The water vapor pressure at the surface, calculated from the ice temperature, indicates a dry atmosphere in early spring, during the recession of the CO_2 ice cap. The large amount of water vapor released by the sublimation of warm frost cannot stabilize subsurface ice at mid-latitudes.

Plain Language Summary During spring, parts of the Martian surface at mid and high latitudes are covered by a thin, bright layer of frost. Some of these ice deposits are made of CO_2 ice, but some frosts have a temperature that is too warm to be CO_2 frosts and are thus constituted of water ice that forms in winter and sublimes in spring. We conducted a spatial and temporal mapping of these ice deposits using the camera THEMIS onboard the Mars Odyssey orbiter to better characterize the exchange of volatiles between the Martian atmosphere and the surface. Water ice is preferentially detected on pole-facing slopes rather than flat surfaces below 45° latitude and all types of surfaces at higher latitudes. In late spring, water ice cannot melt despite solar heating because it cools down with the release of latent heat. On the other hand, these ice deposits are warm enough to form brines if salt crystals are present at the surface. When the frost sublimes, it serves as a source of water vapor that can diffuse into the ground and recondense to stabilize the permafrost below the surface. However, this effect is not sufficient to stabilize subsurface ice at low latitudes.

1. Introduction

Although water is a minor component of the Martian atmosphere, the water cycle is one of the most important contributors to the present and past climate of Mars. For example, although the current atmospheric moisture is low (~13 microns precipitable, Smith, 2002), water clouds have a strong influence on the atmospheric dynamics (Madeleine et al., 2012; Navarro et al., 2014; Wilson et al., 2007, 2008). Similarly, the presence of water ice buried in the subsurface has a significant impact on the surface energy balance, delaying or even preventing CO_2 condensation in winter (Haberle et al., 2008). Therefore, characterizing the mechanisms controlling the water cycle is crucial to better understand the climate on Mars. This water cycle is mainly driven by the sublimation cycle of massive water-ice deposits located primarily at the North Pole and to a lesser extent at the South Pole, although the role of the regolith in this cycle remains controversial (see a full discussion in Montmessin et al., 2017). Every summer, the northern polar water ice cap sublimes, releasing water vapor that is then transported to lower latitudes. Depending on temperature and humidity conditions, this water vapor can condense

in the atmosphere and form clouds (e.g., Curran et al., 1973), diffuse into the subsurface (e.g., Schorghofer & Aharonson, 2005), or form frost on the surface (e.g., Svitek & Murray, 1990).

The characterization of surface water frost deposits is of great interest to assess (a) the exchanges between perennial water ice reservoirs at the poles and the rest of the planet (Bapst et al., 2015), (b) their potential to form liquid water or brines on the surface (e.g., Schorghofer, 2020), (c) their contribution to current surface processes (e.g., Diniega et al., 2021; Dundas, Becerra, et al., 2021), and (d) the exchanges of water vapor between surface frost and subsurface water ice buried in the mid and high latitudes (e.g., Bapst et al., 2015; Lange, Forget, Vincendon, et al., 2023; Williams et al., 2015). Since Leighton and Murray (1966)'s pioneering work on volatile exchanges between reservoirs, local approaches at lander landing sites (Landis, 2007; Martínez et al., 2016; Svitek & Murray, 1990), or globally from orbit (Appéré et al., 2011; Bapst et al., 2015; Carrozzo et al., 2009; Kereszturi et al., 2011; Kieffer & Titus, 2001; Landis, 2007; Piqueux et al., 2008; Schmidt et al., 2009; Schorghofer & Edgett, 2006; Stcherbinine et al., 2023; Titus et al., 2003; Vincendon, 2015; Vincendon, Forget, & Mustard, 2010) have been undertaken to map and characterize water frost deposits. For the latter approach, two methods exist to date: (a) spectroscopic detections of water ice based on near-infrared spectral absorptions (Kereszturi et al., 2011; Langevin et al., 2007; Schmidt et al., 2009; Vincendon, 2015; Vincendon, Forget, & Mustard, 2010) and (b) the identification of bright patches with a temperature that is too warm to be CO_2 ice but is instead H_2O ice (Bapst et al., 2015; Kieffer & Titus, 2001; Piqueux et al., 2008; Schorghofer & Edgett, 2006; Stcherbinine et al., 2023; Titus et al., 2003). This last technique requires simultaneous measurement in visible wavelengths, to detect frost through its distinct albedo or color, and at infrared wavelengths, to determine the composition of the ice through its temperature. This last quantity is required to determine the composition of the ice detected via a bright pattern in the visible range. For instance, Schorghofer and Edgett (2006) identified bright white patches on pole-facing slopes at low latitudes. While their thermal models suggest that this ice was indeed CO_2 ice, they were only able to definitively show that some bright patterns were indeed CO_2 frost via temperature measurements of these slopes. As shown by Vincendon et al. (2014) and Vincendon (2015), although some bright deposits are located on slopes where CO_2 ice is predicted by the models, spectroscopic measurements show that they can sometimes actually be composed of water ice instead of CO_2 ice. Thus, the observation of bright deposits on slopes and correlation with model prediction is not sufficient to demonstrate with certainty the nature of the ices observed.

The coincident acquisition of visible and temperature data enables us to distinguish CO_2 versus H_2O ices, and to document new properties for Mars such as:

1. The temperature of water ice. This measurement can be used to constrain the thermo-physical properties of ice through its diurnal/seasonal evolution (e.g., Bapst et al., 2019), or to determine whether ice can reach melting temperature. However, most of these measurements have been acquired on the massive, perennial water ice deposits at the poles, where temperatures barely exceed 200 K (Bapst et al., 2019; Kieffer & Titus, 2001; Piqueux et al., 2008; Titus et al., 2003). Bapst et al. (2015) have measured ice temperatures down to ±45° latitude with the Thermal Emission Spectrometer (TES, Christensen et al., 2001) and found higher water frost temperature (~220–240 K). However, they acknowledged that these warm-water ice temperatures might be due to sub-pixel terrain mixing (TES has a resolution of ~3 × 6 km) and uncertainty in the retrieved surface temperatures (Bapst et al., 2019). Carrozzo et al. (2009), through a spectroscopic study, have detected water ice at tropical latitudes, which exhibits high temperatures (most between 180 and 245 K, up to 260 K for few detections). Vincendon, Forget, and Mustard (2010) and Vincendon (2015) have extended their study, also detecting water frost on pole-facing crater slopes at tropical latitudes, but they did not retrieve the temperatures of these deposits.
2. The near-surface water vapor content. This quantity, while crucial for the stability of subsurface ice (Schorghofer & Aharonson, 2005) or to constrain the vertical profile of water vapor in the lower atmosphere (Leung et al., 2024, and references therein), has not been directly measured by any rover or lander to date. It has been indirectly derived from simultaneous measurements of relative humidity, temperature, and pressure measurements at the Phoenix (Fischer et al., 2019; Zent et al., 2010), Mars Science Laboratory (Harri et al., 2014), and Mars 2020 (Polkko et al., 2023) landing sites. However, if water frost is present at the surface, the water vapor content at the surface can be directly constrained as the vapor pressure is equal to the vapor pressure over ice at saturation $p_{sat,ice}$ (Pa), which is a function of the ice temperature T_{ice} (K) (Murphy & Koop, 2005):

$$p_{\mathrm{sat,ice}} = \exp\left(-\frac{6143.7}{T_{\mathrm{ice}}} + 28.9074\right) \quad (1)$$

Therefore, determining water ice temperatures could provide a new, broader set of near-surface water vapor data. Yet, this analysis has not been conducted by studies measuring water ice temperatures (e.g., Bapst et al., 2015, 2019; Kieffer & Titus, 2001; Piqueux et al., 2008; Titus et al., 2003).

Here we extend the previous studies on the presence of water frost on the Martian surface by presenting a new data set of water ice observed at mid and high latitudes and by providing a unique data set of water ice temperature and vapor pressure using measurements from the Thermal Emission Imaging System (THEMIS, Christensen et al., 2004) onboard Mars Odyssey. The latter simultaneously combines visible and infrared measurements, enabling the detection and characterization of ice as performed by Titus et al. (2003), Piqueux et al. (2008), and Wagstaff et al. (2008) for water ice; Khuller, Christensen, Harrison, and Diniega (2021) and Lange et al. (2022) for CO_2 ice. Titus et al. (2003), Piqueux et al. (2008) and Wagstaff et al. (2008) focused their studies on the detection of water ice at high latitudes (at the South Pole and above 60°N respectively). Here we propose to extend their approach to the entire planet.

High-resolution imagery allows the detection of small deposits of water ice found at low latitudes (Carrozzo et al., 2009; Vincendon, 2015; Vincendon, Forget, & Mustard, 2010), previously inaccessible to Kieffer and Titus (2001) and Bapst et al. (2015) studies, and reduces uncertainty induced by sub-grid mixing. In addition, measuring ice temperatures reveals whether ice can melt or form brines and constrain the near-surface water content. These data can also validate water frost predictions made by the Mars Planetary Climate Model (PCM, Forget et al., 1999; Lange, Forget, Dupont, et al., 2023). This model, along with the processing of THEMIS data, is presented in Section 2. The results on water frost spatio-temporal distribution, temperatures, and derived near-surface water vapor are described in Section 3. Section 4 focuses on the discussion of these results, and the conclusions are summarized in Section 5.

2. Methods

2.1. THEMIS Data Set

This study uses coincident visible and thermal observations acquired by THEMIS. We recall here the description of the image processing at visible and infrared wavelengths provided by Lange et al. (2022). The THEMIS visible camera has five filters with band centers located at 425 (band 1), 540 (band 2), 654 (band 3), 749 (band 4), and 860 nm (band 5) (Christensen et al., 2004). We use colorized images that are either conventional "RGB" composite resulting from band 4 (or, if not available, band 3), band 2, and band 1 in the blue channel (Bennett et al., 2018; Murray et al., 2016); or "R2B" images, a colorized product where of band 4 (red) and band 1 (blue) are combined using 0.65 × band 1 + 0.35 × band 4 to generate a simulated green band used for the RGB composite (Bennett et al., 2018; Murray et al., 2016).

Surface temperatures are derived from THEMIS band 9 centered at 12.57 μm because of its good signal-to-noise ratio and because it is low sensitivity to atmospheric effects (Fergason et al., 2006; Pilorget et al., 2013). The precision of the measurement is ∼0.5–1 K (Christensen et al., 2004) with an absolute accuracy of ∼2.8 K at 180 K (Fergason et al., 2006), a common temperature for water frost (see Section 3.2). We use the Projected Brightness Temperature product provided on the Planetary Data System (PDS) (P. R. Christensen, 2002). No atmospheric correction is made here. However, as shown in Section 3.2, most of the images are taken between 6 and 9 a.m. and 4 and 8 p.m., when the contrast between atmospheric temperature and the surface is small, and thus when the atmospheric correction should be small.

THEMIS visible wavelength images are characterized by a footprint of ∼18 km wide on the ground (18 m resolution), smaller than the ∼32 km wide swath of the infrared data. Therefore, infrared data are cropped to the extent of the overlapping visible wavelength data. Infrared images display a resolution of 100 m/pixel. Visible images are therefore "degraded" by performing a bilinear interpolation of the visible image grid to the infrared image grid.

Data analyzed here have been acquired during the daytime, with a local time varying from 5 a.m. to 7 p.m., to have a clear image of the surface at visible wavelengths. We only analyze the visible images acquired concomitant to

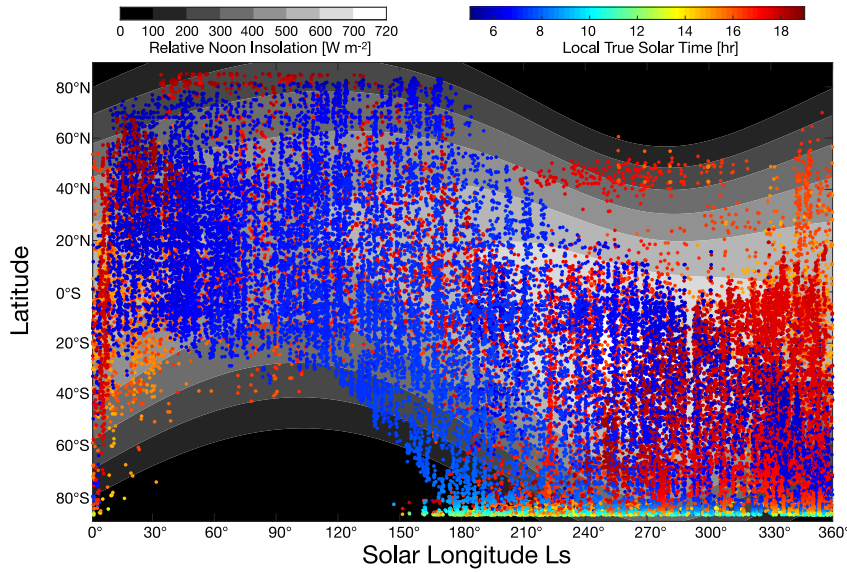

Figure 1. Spatial and seasonal distribution of THEMIS visible/thermal infrared pairs analyzed in this study. The black-white background indicates the seasonality of direct solar illumination (top of the atmosphere) as calculated by a Keplerian orbital model used by KRC (Kieffer, 2013). The *x*-axis represents the solar longitude L_s [°], the Mars-Sun angle, measured from the Northern Hemisphere spring equinox where $L_s = 0°$.

measurements at infrared wavelengths. Some image pairs are disqualified because of (a) calibration issues in both visible and infrared wavelengths, most likely due to the challenging illumination conditions, and (b) unclear surface exposure due to the presence of clouds/dust. The complete data set, presented in Figure 1, represents 39,496 images.

The data set analyzed in this study presents some bias caused by operational, local weather, and illumination constraints (e.g., fewer images are taken in the northern latitudes during the second part of the Martian Year [MY] as the sky is dustier (Montabone et al., 2015), challenging the observations of the surface). The data set exhibits a strong asymmetry in the coverage of the Northern and Southern Hemispheres, thus making a comparison between the two hemispheres difficult. Also, few measurements were made during the autumn/winter at mid and high latitudes, preventing the study of condensation of water frost during this period.

2.2. Water Frost Identification

The identification of water frost is done in two steps, beginning with looking at visible images. Snow or glacier water ice is associated with a high albedo at visible wavelengths, with a spectral slope from blue to red, in contrast to the low albedo of the Martian bare surface (Flanner et al., 2021; Khuller, Christensen, & Warren, 2021; Murchie et al., 2019; Putzig et al., 2005; Singh & Flanner, 2016; Singh et al., 2018, and references therein). For this reason, we similarly anticipate pure CO_2 or H_2O ice to appear as blue-white patches on the brown Martian surface. Hence, we first look at all the visible images and manually flag all the pixels that appear blue-white and which could be interpreted as frost. One of the key limits of this approach is that some thin frost layers might not appear blue-white on THEMIS images and would not be detected with our method. Here, we assume that water frost appears blue-white if its thickness is at least 20 μm. Such thickness is consistent with the work of Svitek and Murray (1990), who showed that the white surfaces appearing on Viking images are associated with such frost thicknesses, and with the laboratory work of Yoldi et al. (2021), who showed that a thickness of 20–30 microns of water frost quintuples the reflectivity of the surface in the blue band and doubles it in the red band (see their Figure 7). A similar detection threshold was also found in Spadaccia et al. (2023). We acknowledge that this empirical threshold limit should also depend on the ice crystals' size, the frost's dust content, the emission angle of the observations, etc (Pommerol et al., 2013). This might explain why our threshold is underestimated: as shown in Section 3.1.1, according to the Mars PCM, frosts detected with THEMIS are mostly thicker than 100 μm (with a few frosts in the 20 and 100-micron range).

Although frost/ice detection based on the bright blue-white color contrasting with the bare surface has been widely used in the past (e.g., Bapst et al., 2015; Calvin et al., 2015; Dundas et al., 2019; James et al., 1979; Lange et al., 2022; Schorghofer & Edgett, 2006), this technique, which is also used in this study, has some important limitations worth mentioning. First, Khuller, Christensen, and Warren (2021) have shown that the albedo of water snow/ice can be drastically reduced if it is contaminated by dust (e.g., less than 1% dust contamination). Hence, dusty frost could be missed with this approach because of the small contrast between this dirty ice and the bare ground. To mitigate this effect, we have stretched the visible images to enhance the color contrast and to help the detection of small patches of frost in relatively low-illuminated areas (e.g., pole-facing slope during the autumn). Second, as noted by Dundas et al. (2019) and Lange et al. (2022), relatively blue lithic material can be misunderstood as frost with our approach. While most of the blue-white units we identified are confidently attributed to ice based on their sharp boundaries following topography, preferential slope orientation, or morphology, we leveraged the few uncertain detections by looking at summer images taken at the same locations to see if the blue-white patches were still present. Another possibility was to confirm the icy nature of these pixels by performing an analysis of the spectral properties with all THEMIS bands (as made for instance by Khuller and Christensen (2021), with the High-Resolution Imaging Science Experiment (HiRISE) data set), but the large number of pixels analyzed here prevent a manual check of all the spectra. Finally, haze/clouds, which can also appear as blue-white on THEMIS visible images (see for instance McConnochie et al., 2010) sometimes induce false positive detections. However, in this case, these bright features appear to be independent of the surface topography, which enables their removal with confidence.

To flag pixels as frost, based on their color, we first apply an initial filter to isolate all pixels with a blue-white color. This method eliminates most of the non-frosted pixels. Next, ambiguous pixels (e.g., bright pixels on a slope exposed to sunlight that appear yellow-white) are eliminated manually. Finally, a last check is made between the raw image and the selected pixels to ensure that no frosted areas have been overlooked. However, we acknowledge that this may result in some frosted pixels being omitted.

At this step, 2,343 images (and nearly 9×10^7 pixels) are flagged as images showing frost. The second step is to now distinguish between CO_2 and H_2O frost. As CO_2 is the main component of the Martian atmosphere, the formation of CO_2 frost is not diffusion-limited. As such, CO_2 frost forms when the surface temperature reaches the temperature of condensation of CO_2, T_{CO_2} [K], given by the Clapeyron law (James et al., 1992):

$$T_{CO_2} = \frac{3182.48}{23.3494 - \ln(P)} \tag{2}$$

with P the local CO_2 partial pressure taken as 0.96 of the total surface pressure (expressed in mbar) derived from the local topography and parameterized surface pressure observations (Withers, 2012). T_{CO_2} ranges from 130 K at the top of Olympus Mons to more than 153 K in Hellas basin (Piqueux et al., 2016). If CO_2 ice is present on the surface, the temperature must be at T_{CO_2}. On the contrary, the formation of H_2O frost is limited by diffusion and is controlled by the partial pressure of H_2O at the surface and the near-surface atmosphere. Water frost can thus exhibit a surface temperature much higher than T_{CO_2}. Therefore, for each pixel flagged as frost, we compare its surface temperature given by the THEMIS infrared measurement with T_{CO_2} (Figure 2b). To account for the instrument noise and possible atmospheric contributions, we assign a 5 K tolerance on this criterion as in Lange et al. (2022). In other words, a pixel is considered as water frost if its temperature T_{ice} is higher than $T_{CO_2} + 5$ K. In comparison, Pilorget et al. (2013) used a 6 K margin, and Khuller, Christensen, and Warren (2021) a 7 K margin. Using these tolerances yields a reduction of the number of water ice detections by 1.6% and 3.8% respectively. With this approach, we exclude water frost at very low temperatures that might be mixed with CO_2 frost and thus consider only "pure" water frost (although dust might be incorporated). For this reason, frost/ice will now only refer to water frost/ice in the rest of this manuscript.

Occasionally, some temperature measurements are associated with large uncertainties (e.g., all measurements above 170 K on the seasonal CO_2 ice cap, Wagstaff et al., 2008). This overestimation is well-characterized and linked to the image calibration protocol that uses a reference image unsuitable at high latitude during winter/early spring (see a complete description of this issue in Wagstaff et al., 2008), and has been mitigated with the new calibration of PDS products since their work. Such images, where the CO_2 ice cap is associated with unrealistic high temperatures (here taken as 160 K) are manually removed from our data set.

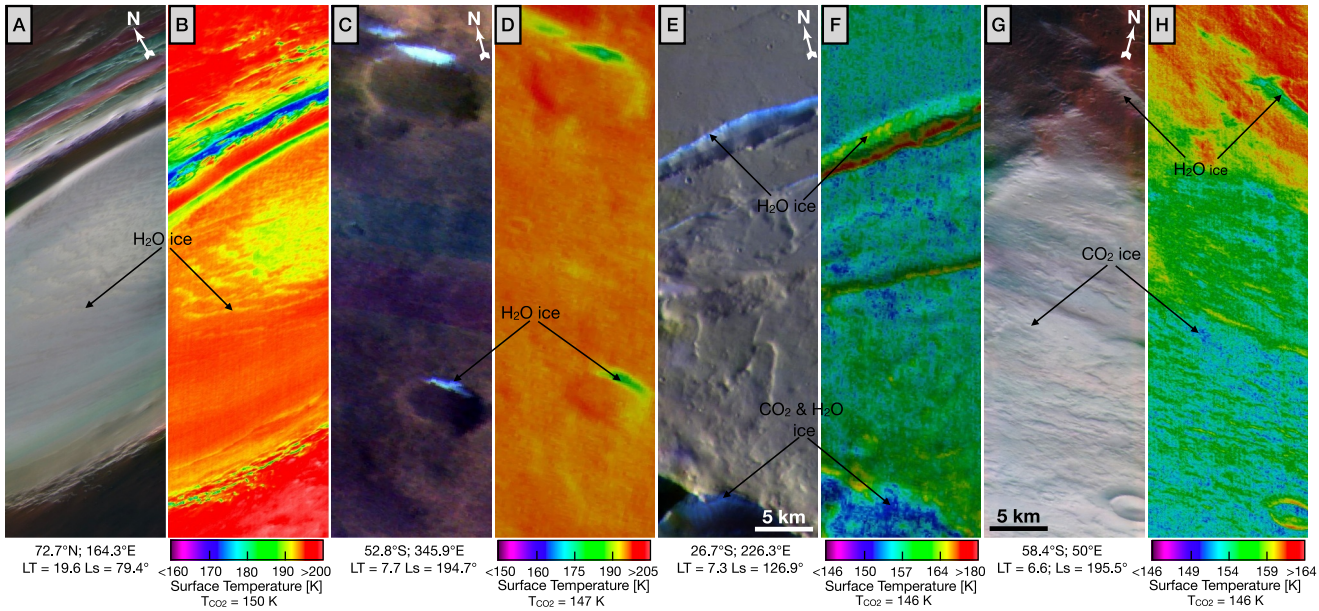

Figure 2. Examples of water ice detections with THEMIS visible wavelength images (a, c, e, g) and corresponding thermal infrared (b, d, f, h) images. Coordinates, solar longitude L_s, local true solar time (LTST), and temperature of condensation of CO_2 are given in the different panels. Blue-white pixels in visible wavelength images with a temperature that is green/yellow/red in the infrared images can be associated with water ice. The white arrows on the upper right of each visible-wavelength image point to the North. Thermal infrared images are underlain with a MOLA background to enhance topography (Zuber et al., 1992). Some terrains appear black in the thermal infrared images because of the background mosaic (not because of an absence of measurement). (a, b) Extract from the images V62050008/I62050007, consistent with perennial water ice. Water ice pixels on the complete THEMIS image (and not just the extract presented here) have a mean temperature of 199.33 ± 5 K at 1-σ. (c, d) Extract from the images V64882003/I64882002, identified as seasonal water ice. Water ice pixels on the complete THEMIS image have a mean temperature of 191.3 ± 3.3 K at 1-σ. (e, f) Extract from the images V63327007/I63327006, where seasonal water ice (upper part of the image) and diurnal CO_2 ice (on the crater rim at the bottom) are present. Water ice pixels on the complete THEMIS image have a mean temperature of 158.1 ± 4 K at 1-σ. (g, h) Extract from the images V56557003/I56557002, where seasonal water ice is present next to the CO_2 ice cap (outside the visible image frame). Water ice pixels on the complete THEMIS image have a mean temperature of 155.9 ± 3 K at 1-σ. The contrast on visible images has been manually increased to highlight the frost.

At the end of the processing, 2,006 images (and 5.3×10^7 pixels) are found to be associated with water frost (e.g., Figure 2). The reader is referred to Khuller, Christensen, Harrison, and Diniega (2021) and Lange et al. (2022) for a mapping of CO_2 frost with the THEMIS data set. As a preliminary validation, we have checked that perennial water ice deposits (North Cap, Korolev crater, Lyot crater, etc.) are well identified by this method (e.g., Figures 2a and 2b). The good agreement between our detection method and the other data sets, as well as the PCM, allows us to be confident in the validity of our detection method (Section 3).

2.3. The Mars Planetary Climate Model

Observational data are compared to the simulations from the Mars Planetary Climate Model, formally known as the LMD Mars Global Climate Model (Forget et al., 1999). In this study, we use the version that models slope microclimates and simulates the condensation of CO_2 and H_2O on slopes (Lange, Forget, Dupont, et al., 2023). Surface properties (albedo, emissivity, thermal inertia) are set to the observations from TES (see Table 2 of Lange, Forget, Dupont, et al., 2023). Seasonal dust opacity profiles are set to an average of the available observations of dust from MY 24, 25, 26, 28, 29, 30, and 31 outside the global dust storm period (Montabone et al., 2015). The representation of the water cycle, detailed in Navarro et al. (2014) and Naar et al. (2021), has been validated through comparison with TES data. A complete description of the surface energy budget, accounting for visible and infrared radiation, soil conduction, and sensible and latent heat fluxes can be found in Lange, Forget, Dupont, et al. (2023).

2.3.1. Modeling the Formation and Sublimation of Water Frost

Three kinds of models are used to simulate the evolution of water ice (see a complete review in Khuller & Clow, 2024). One of the most common approaches (e.g., Bapst et al., 2019; Bramson et al., 2019; Dundas & Byrne, 2010; Kite et al., 2013; Williams et al., 2008) is to sum the sublimation of water ice induced by the

buoyancy of near-surface air, especially given the contrast of mass between the CO_2 gas (molar mass of 44 g m^{-3}) and H_2O (molar mass of 18 g m^{-3}) (Ingersoll, 1970; Khuller & Clow, 2024; Schorghofer, 2020), known as "free convection" (referred to below as "water buoyancy"), and the one driven by wind advection, known as "forced convection." Yet, as shown by Khuller and Clow (2024), these kinds of models have several limitations, including:

- wind-shear and buoyancy terms should not be summed, since they represent two distinct atmospheric regimes. As such, the sublimation rate may be overestimated when summing these two terms;
- ignoring the physical processes in the near-surface and interfacial layers. In the interfacial layer, viscous effects reduce the sublimation rate. While it has a significant effect on Earth (Fitzpatrick et al., 2019), almost none of the models used on Mars today account for this effect. In the surface layer, gustiness induced by large-scale transient convective structures under convective conditions adds shear stress which can promote the sublimation of water ice. Thus, even in the absence of a geostrophic/local wind, the "free convection" regime cannot be achieved, as convective cells will generate a gustiness wind close to the surface.

Hence, as shown by Khuller and Clow (2024), models which sum the wind-shear and buoyancy terms and neglect the physical processes in the near-surface and interfacial layers may inaccurately estimate the sublimation rates. Here, we simulate the evolution of water ice using a common approach in near-surface atmosphere modeling known as the "bulk method" (Colaïtis et al., 2013; Flasar & Goody, 1976; Haberle et al., 2019; Montmessin et al., 2004; Navarro et al., 2014; Savijärvi, 1995), which relies on the Monin-Obukhov theory widely validated on Earth (Foken, 2006), and which can be transposed on Mars (Martínez et al., 2009).

The evolution of the mass of H_2O frost m_w (kg m^{-2}) is computed with:

$$\frac{\partial m_w}{\partial t} = \rho C_q U\left(q_w - q_{sat}(T_{\text{surf}})\right) \tag{3}$$

where ρ (kg m^{-3}) is the air density, U (m s^{-1}) is the wind velocity obtained by combining the large-scale (synoptic) wind near the surface with a wind gustiness induced by buoyancy (Colaïtis et al., 2013), q_w (kg/kg) is the mass mixing ratio of water vapor in the first layer of the model ($z_1 \approx 4$ m), q_{sat} (kg/kg) is the saturation mass mixing ratio computed from the surface temperature (see Equation 1 of (Pál et al., 2019)). C_q (unitless) is a moisture transfer coefficient given by (Colaïtis et al., 2013):

$$C_q = f_q(Ri)\left(\frac{\kappa^2}{\ln\left(\frac{z_1}{z_0}\right)\ln\left(\frac{z_1}{z_{0q}}\right)}\right) \tag{4}$$

where $f_q(Ri)$ (unitless) is a function of the Richardson number Ri (unitless), κ (unitless) is the von Kármán constant set to 0.4; z_0 (m) is the aerodynamic roughness coefficient extracted from Hébrard et al. (2012), z_{0q} (m) the moisture roughness length. $f_q(Ri)$ amplifies the flux for an unstable atmosphere, while it reduces it for a stable atmosphere. The Richardson number Ri is the ratio of the buoyancy term to the flow shear term, and depicts the stability of the atmosphere:

$$Ri = \frac{g}{\theta_s}\frac{(\theta - \theta_s)\,z}{U^2} \tag{5}$$

where g (m s^{-2}) is the gravity field, θ_s (K) is the surface temperature, θ (K) is the potential temperature at altitude z (m). $Ri = 0$ for a neutral atmosphere, $Ri < 0$ for an unstable atmosphere, $Ri > 0$ for a stable atmosphere. The stability functions $f_q(Ri)$ used are the ones from England and McNider (1995). The stability functions used for the moisture are the same as for the heat as it is a consistent assumption validated with Earth experiments (e.g., Jiménez et al., 2012, and references therein). These functions have been well-validated on Earth, in Antarctica (Vignon et al., 2016), and have significantly improved the predictions of the near-surface environment on Mars, especially during the daytime, when the near-surface atmosphere is unstable (Colaïtis et al., 2013).

z_{0q}, which represents the viscous effects in the interfacial layer, is parameterized as the thermal roughness length given by Brutsaert (1982):

$$z_{0q} = z_0 \exp\left(-7.3\kappa \mathrm{Re}^{1/4}\mathrm{Pr}^{1/2} + 5\kappa\right) \quad (6)$$

where Re (unitless) is the Reynolds number derived from the wind, density, and viscosity given by the model in the near-surface layer, Pr (unitless) the Prandtl number derived from kinematic viscosity and thermal diffusivity in the model. The application of this parameterization to the Martian surface layer has been discussed by Martínez et al. (2009). In our simulations, z_{0q} is nearly 1/10 of z_0. Given the low Reynolds number on Mars (global -over the planet-mean value of 1.7 over the year in our simulations), the approximation that the moisture roughness length is equal to the thermal roughness length is relevant (Larsen et al., 2002).

One of the key assumptions in our model is that the stability of the atmosphere only depends on the thermal contrast between the atmosphere and the surface, and the instability induced by the difference of molar weight between H_2O and CO_2 (Ingersoll, 1970; Khuller & Clow, 2024; Schorghofer, 2020) is not considered in the stability functions and the computation of the gustiness. We show that this approximation is reasonable for our study below.

2.3.2. Effect of Water Buoyancy on the Atmospheric Stability and the Sublimation Rate

To account for the effect of water buoyancy in the overall buoyancy in the near-surface layer, the definition of the Richardson number Ri (noted Ri_{dry} in this case) can be modified with:

$$Ri_{\mathrm{wet}} = \frac{g}{\theta_{vs}} \frac{(\theta_v - \theta_{vs})z}{U^2} \quad (7)$$

θ_v (K) is the virtual potential temperature defined by:

$$\theta_v = \frac{\theta}{1 - \frac{P_v}{P}(1-\epsilon)} \quad (8)$$

where P_v (Pa) is the partial pressure of water vapor, P (Pa) the total pressure, ϵ the ratio of the molar mass of water vapor v.s. dry air (i.e., CO_2 gas). This quantity represents the temperature that dry air with the same density and pressure as moist air would have. In case ice is present at the surface or at an altitude z, P_v is given by the saturation pressure over ice (Murphy & Koop, 2005).

We present in Figure 3a the wet Richardson number as a function of the surface and atmospheric temperatures, with parameter $U = 10$ m s^{-1} (a typical value during daytime, Martínez et al., 2017), $P = 610$ Pa, the global averaged Martian Pressure, and no water vapor in the atmosphere to maximize the effect of water buoyancy. No significant changes happen when changing the atmospheric humidity from 0 to the current humidity. The stability limit is given by $Ri_{wet} = 0$ (white part in Figure 3a). The dark curve represents the "dry" stability limit (i.e., without the effect of water buoyancy). The wet stability limit at low temperatures agrees well with the dry limit at low temperatures and starts to deviate at ∼240 K. This limit changes slightly by a few kelvins when varying the total pressure P). At high temperatures (≥260 K), the effect of water buoyancy induces a strong instability and surpasses the strong, stable stratification between the warm atmosphere and colder surface. This is mainly due to the exponential dependence of saturation pressure over water ice (Equation 1, Murphy & Koop, 2005), which at warm temperatures, can reach the average surface pressure on Mars. The difference in wind gustiness when accounting for this effect is ∼5 m s^{-1} at 273 K (Khuller & Clow, 2024).

To quantify the effect on the sublimation rate, we first compare $f_q(Ri_{wet})$ and $f_q(Ri_{dry})$, without including gustiness induced by water buoyancy, in Figure 3b. The stability function f_q is barely affected by the effect of water buoyancy, except at high temperatures close to the melting point of water (273.15 K). The buoyancy is mostly dictated by the temperature contrast between the surface and near-surface atmosphere. Yet, when accounting for a gustiness wind $U_g = 5$ m s^{-1} induced by the water buoyancy (Khuller & Clow, 2024), the sublimation rate can increase by 25% (Figure 3c) at low temperatures (which is a bit unrealistic since the atmospheric instability is very weak at these low temperatures, Figure 3a, and the gustiness induced by water buoyancy should be thus much lower), and 100% close to the melting point. Hence, our approximation to neglect the effect of water buoyancy in our simulation is correct a low temperatures (≤240 K). As shown in Section 3.2, this is the range of

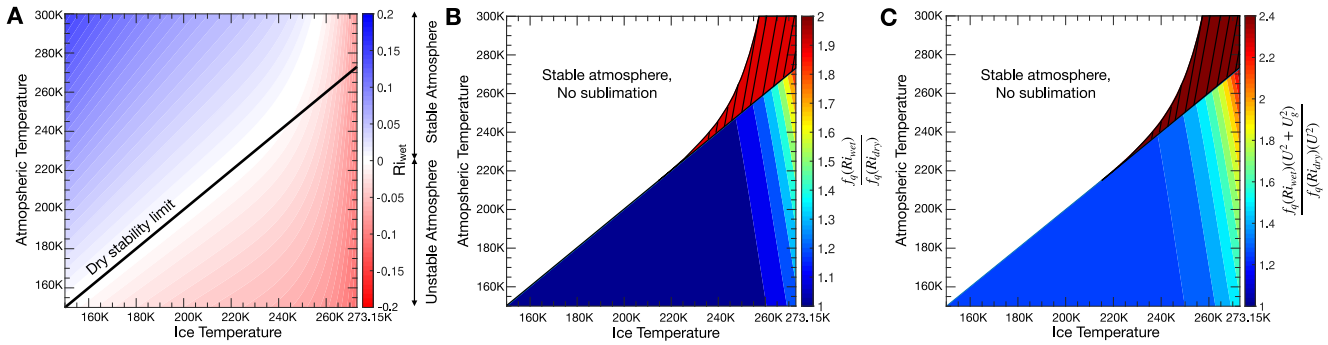

Figure 3. (a) Wet Richardson number as a function of the atmospheric temperature (at 4 m, first atmospheric layer of the Mars PCM) and surface temperature. A negative Richardson number (presented in red in the Figure) indicates an unstable atmosphere. The dry stability limit ($Ri_{dry} = 0$) is indicated by the dark curve. (b) Ratio of the stability function computed with the wet Richardson number and the dry Richardson number. The dashed areas correspond to a stable atmosphere according to the dry Richardson number, where the stability function $f_q(Ri_{dry}) = 0$. In this area, $f_q(Ri_{wet})$ ranges between 1 and 1.2. (c) Ratio of the stability function computed with the wet Richardson and the near-surface wind speed accounting for gustiness induced by water buoyancy (Colaïtis et al., 2013; Khuller & Clow, 2024) with the stability function computed with the dry Richardson and the near-surface wind speed. Dashed lines is not considered for the same reason as in panel (b).

water ice temperatures modeled and measured on Mars. Hence, our results should not be significantly impacted by our assumption to neglect water buoyancy.

2.3.3. Model Validation

As stated in Section 2.3.1, the methods used in this model have been widely used and validated on Earth. On Mars, this model has been successfully applied to simulate the sublimation of the massive perennial water ice deposits at the North Pole and the release of water vapor in the atmosphere (Navarro et al., 2014). The model also agrees well with the observations of water ice exposure close to the CO_2 seasonal cap (Langevin et al., 2007), and the presence of water ice frost on pole-facing slopes at mid-to-low latitudes (Lange, Forget, Dupont, et al., 2023; Vincendon, 2015; Vincendon, Forget, & Mustard, 2010). The sub-grid slope parameterization has been validated with comparisons between the model outputs and surface temperatures measured on slopes by several instruments (Lange, Forget, Dupont, et al., 2023). We present in Figure 4 the H_2O frost thickness at Promethei Terra (32.3°S, 118.6°E) and compare them with observations of frost on the crater rim with high temporal coverage by Vincendon (2015). The good agreement between the model outputs and the observations (which can be generalized to other locations presented in Vincendon, 2015, not shown here) validate our method, the modeled timing of formation/sublimation of the frost, as the modeled frost thickness.

2.3.4. Model Limitations

There are two main limitations in the model used. First, the effect of water buoyancy should be considered. This requires modifying the parameterization of the Planetary Boundary Layer in the Mars Planetary Climate to account for convection driven by H_2O buoyancy (Ingersoll, 1970; Khuller & Clow, 2024; Schorghofer, 2020), CO_2 buoyancy at high latitudes in the polar night (Hess, 1979), and include possible phases changes/latent heat released. This is left as a future work. Furthermore, on slopes, strong slope winds can have a significant impact on surface temperatures (Smith & Spiga, 2018; Spiga & Smith, 2018), and thus should fasten the sublimation of ice. A parameterization of the slope winds in the Mars PCM is under implementation.

3. Results

3.1. Distribution of Frost

3.1.1. Spatial Distribution

The spatial distribution of frost is presented in Figure 5. Water ice is detected down to 21.4°S, 48.4°N. 91% of the low-latitude detections (in the ±45°N band) occur on pole-facing slopes, where water vapor preferentially condenses (Lange, Forget, Dupont, et al., 2023; Vincendon, Forget, & Mustard, 2010). At higher latitudes, 64% of the detections are made on pole-facing slopes. In comparison, Carrozzo et al. (2009) and Vincendon, Forget, and Mustard (2010) have detected water frost on pole-facing slopes down to 15°S and 13°S–32°N respectively using

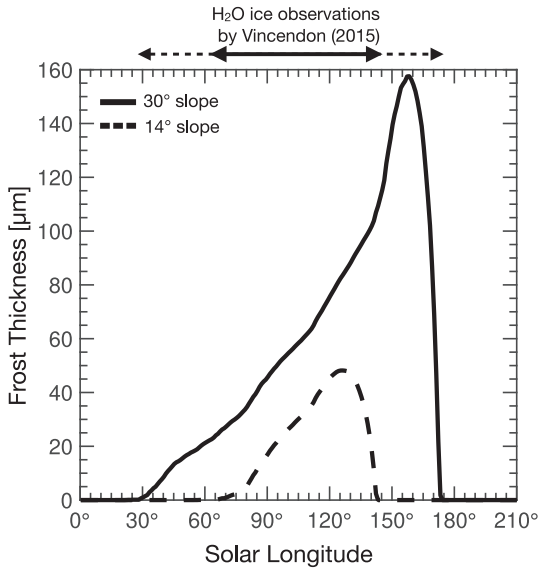

Figure 4. Water frost thicknesses predicted by the Mars PCM at Promethei Terra (32.3°S, 118.6°E) compared to the observations (plain arrow) of water frost by Vincendon (2015) (uncertainty in the detections presented with the dashed arrow).

near-infrared data from OMEGA (Observatoire pour la Minéralogie, l'Eau, les Glaces et l'Activité) and CRISM (Compact Reconnaissance Imaging Spectrometer for Mars) onboard the Mars Reconnaissance Orbiter.

The difference in the latitudinal extent of the frost detected with THEMIS and OMEGA/CRISM can be explained by the intrinsic properties of each data set and instrument. We have estimated the thickness of the frost detected with THEMIS on crater slopes between 50°S and 20°S using the PCM (Figure 6). THEMIS detects water ice with a median thickness of 180 µm (minimum thickness estimated to be near 18 µm). Hence, our approach mainly detects thick frost layers (~100 µm thick), and our detection threshold estimated in Section 2.2 may have been underestimated. In comparison, OMEGA and CRISM have an ice detection threshold of 2–5 µm (Vincendon, 2015; Vincendon, Forget, & Mustard, 2010). At latitudes 10°S–20°S, water ice should be thin (a few tens of microns, see Figure 12 of Lange, Forget, Dupont, et al., 2023). Hence, THEMIS does not seem to be able to detect such thin ice at these low latitudes compared with OMEGA/CRISM.

Between 20° and 50° latitude, the geographic distribution of water frost is consistent with OMEGA/CRISM observations (Vincendon, Forget, & Mustard, 2010). In the South, between 20°S and 30°S, two frost-free areas with no frost are found between 100°E and 210°E and 250°E and 360°E, one of which not observed by Vincendon, Forget, and Mustard (2010). Most of the THEMIS observations obtained in this longitudinal band were acquired before $L_s = 100°$, where frost is expected to be very thin (≤10 µm thick according to models, Vincendon, Forget, & Mustard, 2010; Lange, Forget, Dupont, et al., 2023) and illumination low, especially on pole facing slopes (Figure 1). Hence, frost may be too thin to yield a detectable signature at visible wavelengths, preventing detection with our proposed method. For the 250°E−360°E band, two processes may explain the absence of frost. First, the 250°E−360°E area is characterized by smooth lava terrains with few slopes (Vincendon, Mustard, et al., 2010), while water frost is only stable on steep pole-facing slopes between 20°S and 30°S (Lange, Forget,

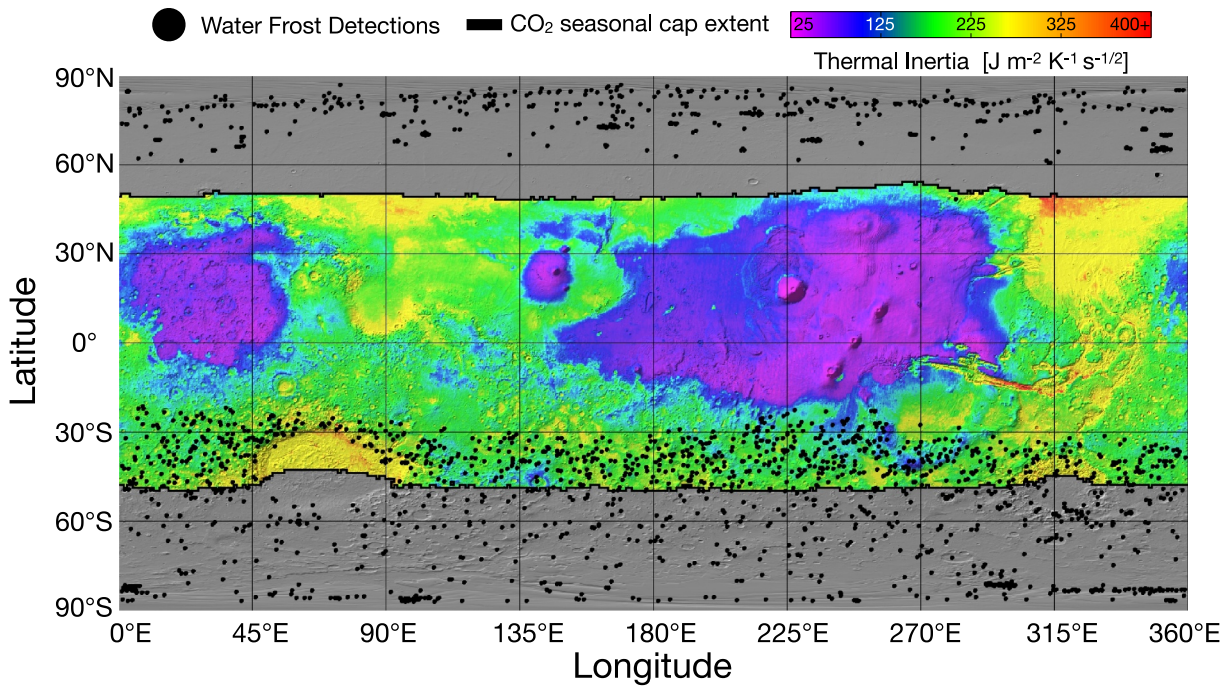

Figure 5. Distribution of water frost detected with THEMIS (black dots). The colorized background is a thermal inertia map from Piqueux et al. (2023) overlain by a MOLA-shaded relief (Zuber et al., 1992), only shown outside the maximum extent of the continuous seasonal caps (Piqueux et al., 2015).

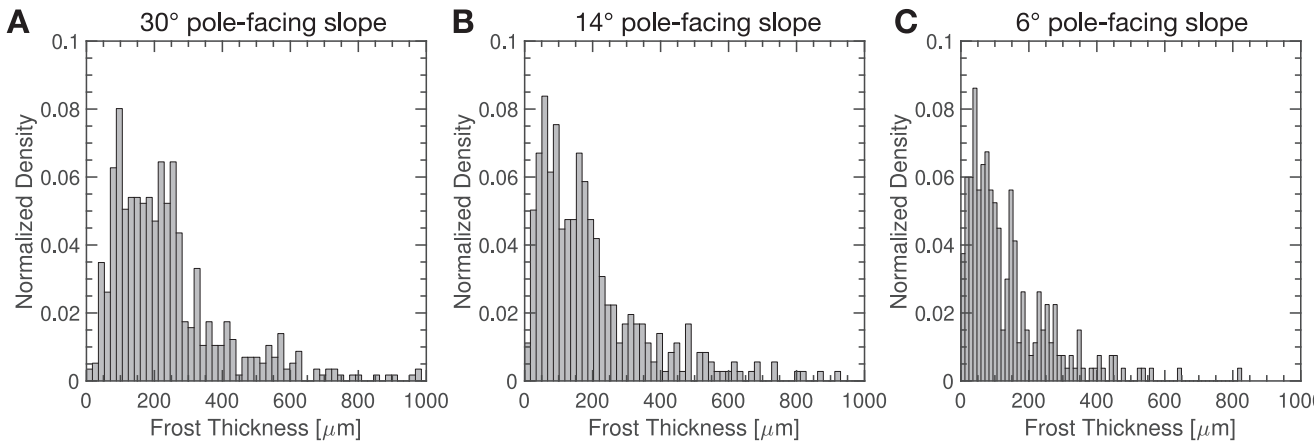

Figure 6. (a) Distribution of water frost thickness detected with THEMIS between 20°S and 50°S as modeled by the Mars PCM. Since most of the detections are made on the top of crater rims, we have derived the frost thicknesses assuming a pole-facing slope of 30°. Cases with modeled frost thickness larger than 1,000 μm are not shown. For completeness, the distribution of water frost thicknesses for a 14° slope (b) and 6° slope (c) is presented. The case for a flat surface is not presented as almost all of the frosts detected in this latitudinal range are on pole-facing slopes.

Dupont, et al., 2023; Vincendon, Forget, & Mustard, 2010). Second, for the 300°E−360°E area, the absence of frost is a consequence of a drier atmosphere induced by a western jet on the eastern side of Tharsis (Joshi et al., 1994, 1995; Lange, Forget, Dupont, et al., 2023; Vincendon, Forget, & Mustard, 2010). Most of the deposits found between 20°S and 30°S are located in the West of Hellas basin, where a southward wet flux of air converges (Figure 7 of Vincendon, Forget, & Mustard, 2010), promoting the formation of water frost at this location. We also note that no water frost detections are made within the Hellas basin. This is mostly due to a stationary wave induced by the strong topographic depression of Hellas, filling the basin with dry air and thus preventing the formation of water frost (Vincendon, Forget, & Mustard, 2010). Challenging conditions (for instance clouds (Kahre et al., 2020; Langevin et al., 2007), suspended dust (Martin & Zurek, 1993), etc.) which prevent a clear view of the surface might also explain the absence of frost detections at this location with our method. For instance, Langevin et al. (2007) have detected some water frost deposits in the South of the basin during spring with OMEGA/CRISM as they do not need a clear exposure of the surface to identify frost. In the North, only one detection is made below 50°N, but this is a consequence of the bias data set used in this study and the sparse coverage of the Northern Hemisphere at mid-latitude during northern winter/spring (Figure 1). At high latitudes, in both hemispheres, no significant frost-free areas can be found.

3.1.2. Temporal Distribution

The temporal distribution of water frost is presented in Figure 7. For completeness, we also present CO_2 ice frost detected with THEMIS data, that is, pixels with a temperature lower than $T_{CO_2} + 5$ K. In the South, equatorward of 50°S, most of the water ice detections are made after the sublimation of the CO_2 seasonal ice on pole-facing slopes. Water frost can survive 10–20° of L_s after the disappearance of CO_2 ice. The same comparison is difficult to make in the North, due to the low number of detections. Summer water ice detections are made where perennial water ice is observed (water ice cap at the North Pole, Korolev crater, etc.).

Bapst et al. (2015) have exhibited a strong hemispheric asymmetry in the presence of water ice frost during autumn. They showed that widespread water ice deposits can be observed in the North during autumn (before $L_s \leq$ 270°), but none were detected in the South during southern autumn (before $L_s \leq 90°$). We report here 27 occurrences (i.e., 1.3% of the data set) of water frost detected during the autumn between 32°S and 23°S, mostly in the West of Hellas basin and at longitudes 200°E−250°E. All of these detections are made on pole-facing slopes. The same detections have been made by Vincendon, Forget, and Mustard (2010). Yet these observations should not contradict Bapst et al. (2015)'s conclusions since (a) they are made on local sites with favorable thermal conditions (steep pole-facing slopes) and (b) they take place at low latitudes, where Bapst et al. (2015) were unable to observe ice/frost due to the resolution of TES, far from the CO_2 seasonal ice cap where they noted this asymmetry.

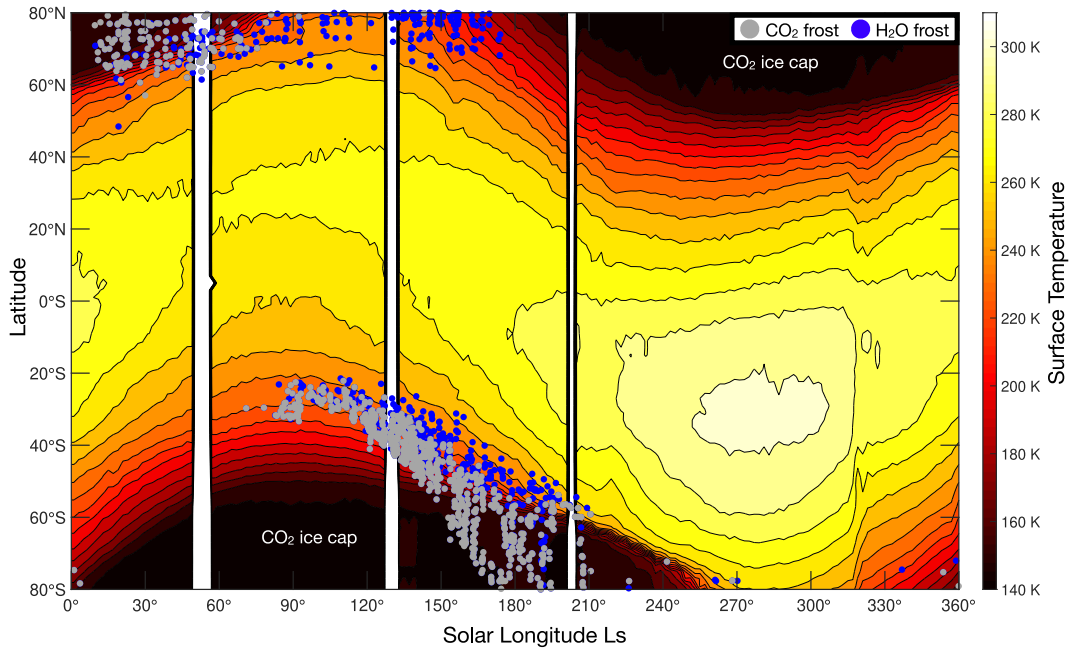

Figure 7. Distribution of water and CO_2 frost. The colorized background is the zonal average surface temperature measured by TES at 2 p.m. during MY 26 (M. D. Smith, 2004). Perennial polar caps at latitudes higher than ±80° are not presented here.

A focus on the water frost evolution at mid-latitudes in the South is presented in Figure 8. Again, this analysis is not performed in the North due to the bias in the distribution of the data set. THEMIS and OMEGA/CRISM data sets have a similar temporal evolution during southern spring (Figure 8). Few detections have been made with THEMIS during the condensation of H_2O ($L_s \leq 120°$) mostly because of the sparse measurements made at this period (Figure 1). Also, at that time, pole-facing slopes are shadowed, preventing a clear exposure of the surface and thus detection of water frost. Finally, ice deposits are expected to be thin during this period (nearly 1–2 μm). Therefore, this low thickness might reduce the albedo contrast between the frost and the defrosted surface, challenging the detection of frost based on our method. Vincendon, Mustard, et al. (2010) also noted that OMEGA/CRISM could only detect frost with a thickness larger than a few microns, possibly explaining the absence of frost detections at $L_s \leq 80°$. The condensation and sublimation timing of H_2O frost deposits detected with THEMIS is consistent with the PCM prediction (Lange, Forget, Dupont, et al., 2023), although the PCM underestimates the sublimation of H_2O by 10° of L_s. It is not clear if the earlier condensation of H_2O frost in the PCM is due to a systematic error in the model or a bias due to the sparse number of detections made at that time.

3.1.3. Retreat of the Water Frost in the Southern Hemisphere

The seasonal evolution of the water frost boundary in the Southern Hemisphere is presented in Figure 9. At $L_s \sim 130°$ the longitudinal extent of water frost is almost homogeneous (mean latitude of 38°S ± 0.9° at 1-σ), except in the west of Hellas which promotes the accumulation of frost as explained in Section 3.1.1. At $L_s \sim 150°$ water frost extends to 45°S ± 1.9° at 1-σ. In the Hellas area, water frost is not present as a consequence of the dryer air in this region (see Section 3.1.1) and observational bias. At $L_s \sim 170°$ water frost extends to 58°S ± 2.9° at 1-σ, except in Hellas where no frost is observed again. Finally, at $L_s \sim 190°$, water extends to 65°S ± 2.9° at 1-σ. The high variability in the latitudinal extent for $L_s = 170°$ and 190° is mostly due to the small number of detections for these L_s (twice less than the number of detections at $L_s \sim 130°$, 150°). For all solar longitudes, the latitudinal variability also results from the variability in surface properties (albedo, thermal inertia) and where frost is detected (flat surface, steep/small slope, etc.).

For both $L_s \sim 170°$ and $L_s \sim 190°$, the latitudinal extent of the H_2O frosts matches the extent of the seasonal CO_2 ice cap (Piqueux et al., 2015). The presence of H_2O ice deposits close to the CO_2 ice cap edge can be explained by either the presence of small impurities of H_2O ice within the CO_2 ice cap or by a water ice annulus, which persists

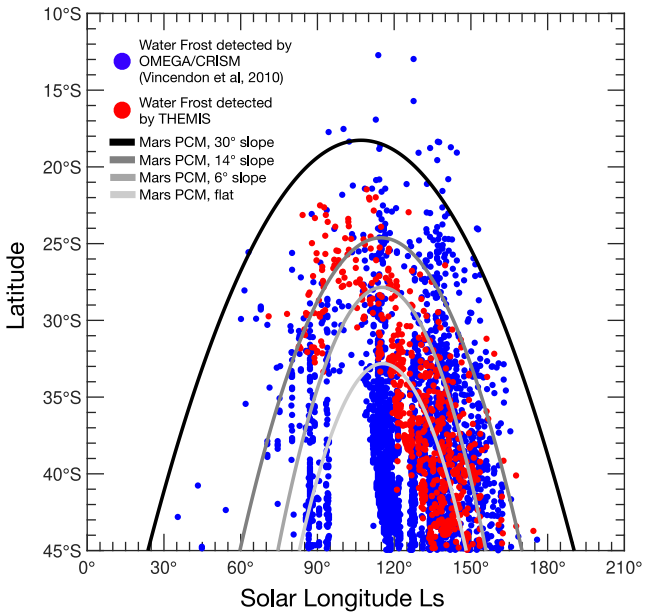

Figure 8. Latitudinal distribution of H_2O frost versus solar longitude L_s. Blue points correspond to the observations of frost with CRISM/OMEGA (Vincendon, 2015; Vincendon, Forget, & Mustard, 2010). Red points correspond to the observations of frost with THEMIS. The dark curve is the prediction of frost stability on a 30° pole-facing slope retrieved from Lange, Forget, Dupont, et al. (2023), as most of the ice deposits are found on the crater rim where the slopes are the steepest. Other predictions for the slopes modeled in Lange, Forget, Dupont, et al. (2023) are given in grays. Following Lange, Forget, Dupont, et al. (2023), H_2O ice is predicted at a given latitude by the PCM if the H_2O frost thickness exceeds 5 μm. The PCM outputs are retrieved at 2 p.m. to be consistent with OMEGA/CRISM local time of acquisitions. Hence, the dark curve represents the stability of seasonal H_2O frost on pole-facing slopes.

after the sublimation of the seasonal CO_2 ice cap, as in the Northern Hemisphere (e.g., Appéré et al., 2011; Bibring et al., 2006; Kieffer & Titus, 2001; Wagstaff et al., 2008). Such a possibility is discussed in Section 4.2.

3.2. Frost Temperature

The distribution of temperature of water ice measured by THEMIS is presented in Figure 10. The mean temperature of water ice measured is 170.9 ± 17 K at 1-σ, with a maximum value of 253.3 K. The two peaks at 160 and 200 K in the distribution of temperatures measured by THEMIS reflect the difference in the nature of the ices observed: The cold peak corresponds to seasonal frosts observed in the morning, after the disappearance of the CO_2 ice, and the hotter peak to warm frosts observed at perennial deposit locations in summer (or to some seasonal frosts observed just before they disappear, at the end of the day). CO_2 frost, misinterpreted as water frost at the level of seasonal ice caps (Section 4.2) also contributes (but to a minor extent) to the cold peak at 160 K.

In comparison, Wagstaff et al. (2008) and Bapst et al. (2015) found temperatures between 165 and 210 K for the water ice deposits in the Northern Hemisphere and up to 240 K for the Southern Hemisphere (Bapst et al., 2015). Water ice temperatures measured by Carrozzo et al. (2009) on pole-facing slopes at tropical latitudes range from 180 to 260 K. The low ice temperature measured in this study is mostly an effect of the local time of the measurements: 75% of the water detections are made between 5 and 9 a.m. and 15% between 5 and 9 p.m. In comparison, most of the detections made by Carrozzo et al. (2009) are between 10 a.m. and 5 p.m. The last detections made during the rest of the day are confined to the South Pole. To quantify the bias induced by the local time, we have compared the measured temperature with the distribution of temperature predicted by the PCM for a complete MY (Figure 10). The water ice thermal properties in the model are a broadband albedo of 0.33, thermal inertia of 800 J m^{-2} K^{-1} $s^{1/2}$, and an emissivity of 1 (Lange, Forget, Dupont, et al., 2023). For this computation, we extracted the temperature predicted in the PCM for a 30° pole-facing slope, equatorward-facing slope, and flat surface only if the model predicts a frost thickness higher than 1 μm for these terrains. The PCM predicts water ice temperatures that are on average 180 ± 21 K at 1-σ, with a maximum temperature of 264.3 K. Hence, frost temperature measured by THEMIS seems to be lower by ∼10 K compared to the model. In both cases, no melting of pure water ice is expected as temperatures are below the triple point of water (273.15 K). A complete discussion on a possible melting is given in Section 4.3.

While pure water ice melting is incompatible with our results, a brine solution could form in the thermal conditions measured by THEMIS. Indeed, the presence of salts in the water ice mixture can reduce the temperature needed to melt to $T_{E,\ Ca(ClO_4)_2}$ = 198 K for Ca-perchlorate, $T_{E,\ Mg(ClO_3)_2}$ = 206 K for Mg-chlorate, $T_{E,\ Mg(ClO_4)_2}$ = 212 K for Mg-perchlorate, and $T_{E,\ Na(ClO_4)_2}$ = 237 K for Na-perchlorate (Chevrier et al., 2022). As the widespread presence of salts and perchlorates on the surface of Mars has been demonstrated (Clark, 1981; Glavin et al., 2013; Hecht et al., 2009; Osterloo et al., 2008, 2010), we can assume that these salts are present where we detect water ice. As shown by Figure 10, some water ice deposits have a temperature higher than eutectic temperatures of Ca-perchlorate (267 detections, e.g. Figures 2b and 2d), Mg-(per)chlorate (respectively 168 and 106 detections), and Na-perchlorate but to a less extent (7 detections). Their location, along with the maximum temperature of these ice deposits, are shown in Figure 11.

Except for 4 images (e.g., Figure 2d), all warm frosts are detected above 60° latitude during summer (e.g., Figure 2b). For each of these sites, we have investigated THEMIS, High-Resolution Imaging Science Experiment (HiRISE, McEwen et al., 2007) and Context Camera (CTX, Malin et al., 2007) data acquired during summer to search for possible indications of fluid flow where frost would have melted into brines. Yet, we do not find evidence of such flow where THEMIS identified warm frosts, even where Kereszturi et al. (2010) and Möhlmann and Kereszturi (2010) have identified flow-like phenomena on dark dune spots at high latitudes that they

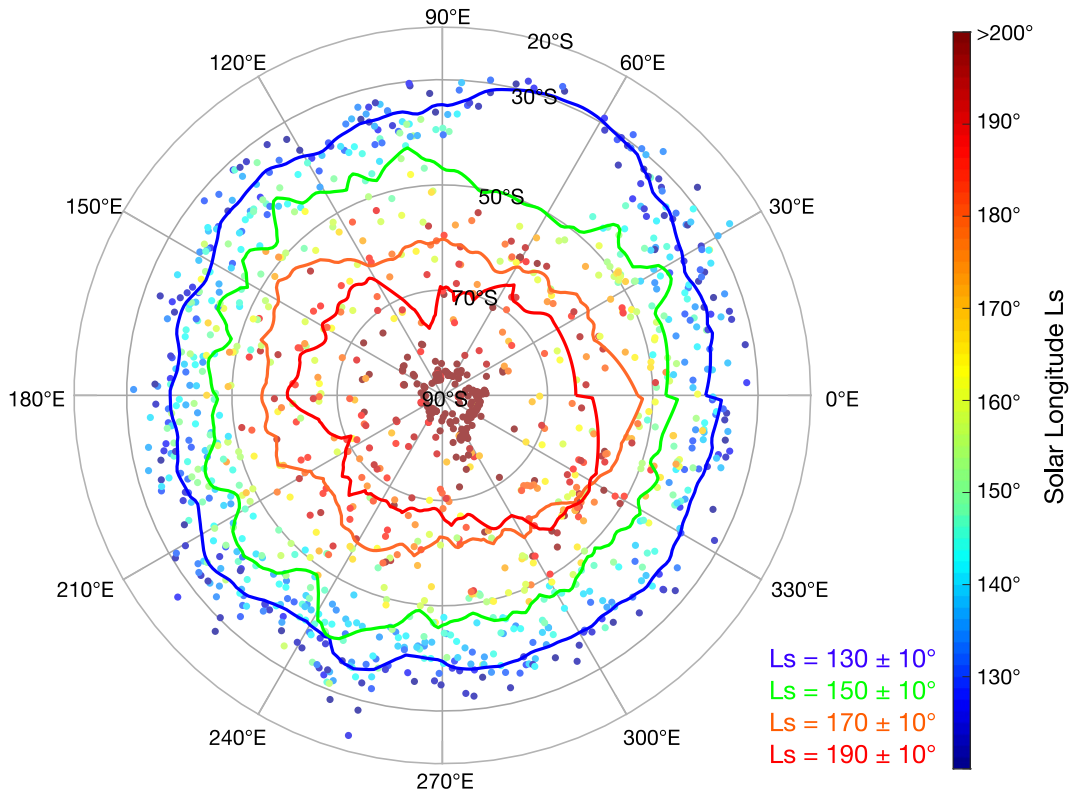

Figure 9. Spatial distribution of discontinuous H_2O frost observed by THEMIS on flat surfaces or slopes in the Southern hemisphere (colored dots). Colors indicate the solar longitude L_s at the time of the acquisition. Plain curves represent median latitudinal distribution of H_2O for $L_s = 130° \pm 10°$ (blue curve), $L_s = 150° \pm 10°$ (green curve), $L_s = 170° \pm 10°$ (orange curve); $L_s = 190° \pm 10°$ (red curve).

attributed to brines. Some dark streak features are observed on some crater slopes (e.g., South, Schmidt craters) but can be explained by other environmental factors such as wind for instance. We speculate that the lack of evidence of brine flow may be due to (a) the actual absence of brines and (b) if a brine does form, the amount of liquid may not be large enough to destabilize the surface material (either through lack of salt or immediate evaporation of the liquid). As water frosts are expected to be thin (from tens of micrometers to a few mm), it is hard to imagine that the brines would form a large flow, but should instead form a few droplets at the surface, which would percolate through the porous regolith. As shown by Schorghofer (2020), the warmest frosts should be located poleward of boulders. Indeed, frost on pole-facing slopes should warm slowly during early spring, while areas behind boulders should warm suddenly during late spring/early summer after being shadowed during part of the year. Yet, THEMIS resolution is not sufficient to observe these locations.

If these ices were to form a brine, their stability would be very limited. As demonstrated by Rivera-Valentín et al. (2020) and Chevrier et al. (2022), brines would be stable for only a few hours a year at mid and high latitudes. Although their model does not consider the thermal effect of slopes, PCM simulations of the slope microclimates show that the temperature of water ice exceeds the eutectic temperature T_E for only a few hours a day and on only a few sols (ranging from 1 to 10 sols). It should be noted that our criterion for stability is solely based on surface temperature, although it also depends on the water activity. A complete study of the stability of brines coupling a complete thermodynamic model and our PCM simulating slope microclimates is left for future work.

3.3. Near-Surface Water Vapor Content

Here we present the near-surface water vapor inferred from temperatures measured with THEMIS. Once T_{ice} has been measured, we derive the near-surface water vapor with Equation 1. Results are presented in Figure 12a. The mean partial pressure derived is $0.05^{+0.2}_{-0.05}$ Pa at 1-σ. The highest partial pressures are found at the poles during summer when perennial water ice caps sublime. Otherwise, most of our near-surface water vapor values are low,

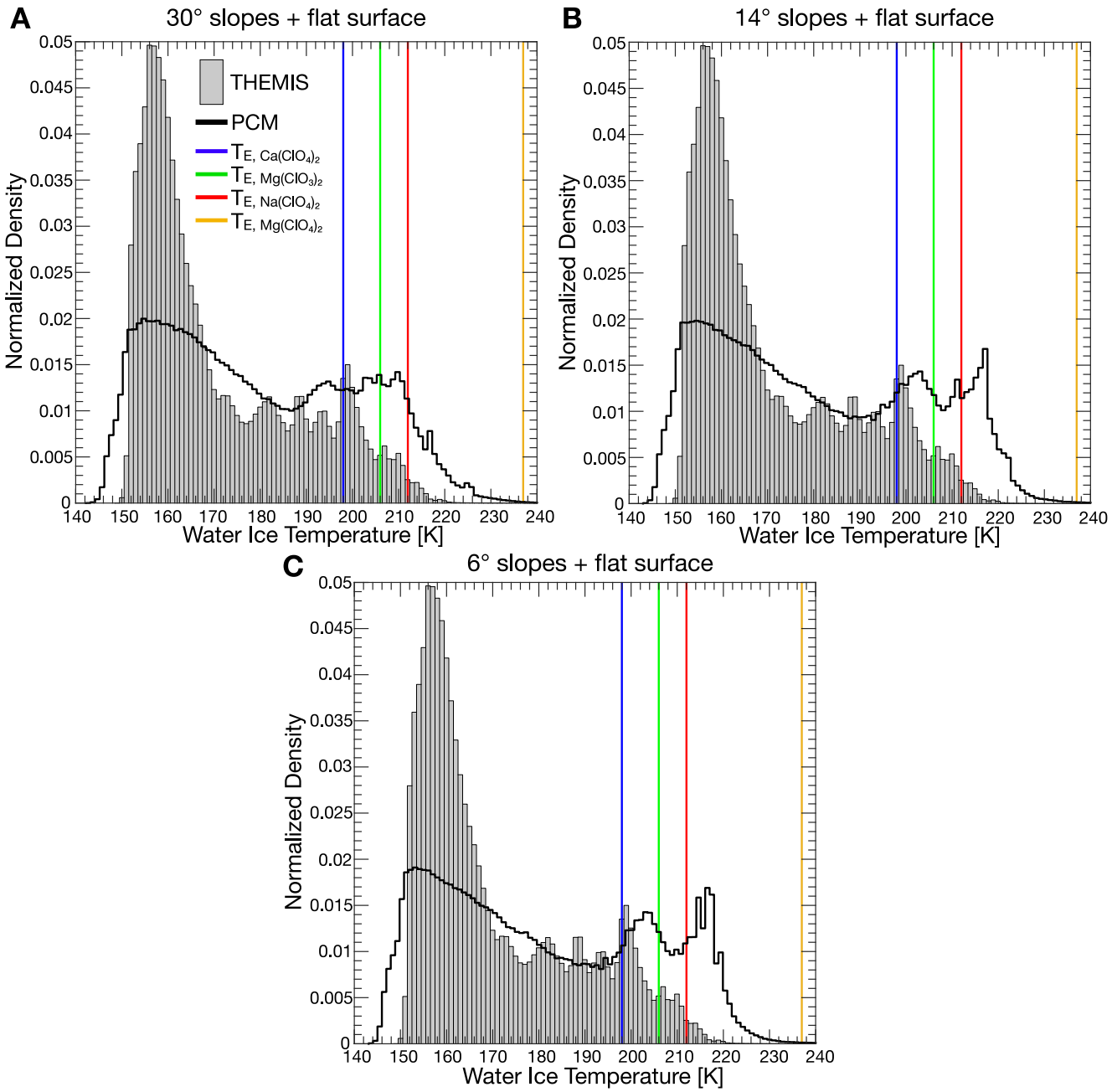

Figure 10. (a) Distribution of water frost temperature measured by THEMIS (histogram) and predicted by the PCM for a flat surface, and 30° North-facing/South-facing slopes (black curve). The distribution has been normalized by dividing each count by the total number of pixels (5.3×10^7 pixels for THEMIS, 3.5×10^6 for the PCM). The eutectic temperature of Ca-perchlorate $T_{E,\ Ca(ClO_4)_2} = 198$ K is represented by the blue curve, the green curve is for the Mg-chlorate ($T_{E,\ Mg(ClO_3)_2} = 206$ (K)), the red curve is for the Mg-perchlorate ($T_{E,\ Mg(ClO_4)_2} = 212$ (K)), and the orange curve is for the Na-perchlorate ($T_{E,\ Na(ClO_4)_2} = 237$ (K)). (b) Same as panels (a), but modeled temperatures are for a flat surface, and 14° North-facing/South-facing slopes. (c), but modeled temperatures are for a flat surface, and 6° North-facing/South-facing slopes.

mostly because measurements are made during the early stage of the ice sublimation, early in the morning or late afternoon, when ice temperatures are low.

We have nevertheless checked the consistency of our results with TES measurements of water vapor column-abundance (Smith, 2002). These measurements first need to be interpolated from column-abundance to near-surface. However, such an operation is not easy as the vertical structure of the water vapor in the lowest layer of the atmosphere is not very well constrained (Leung et al., 2024; Tamppari & Lemmon, 2020). We used here the

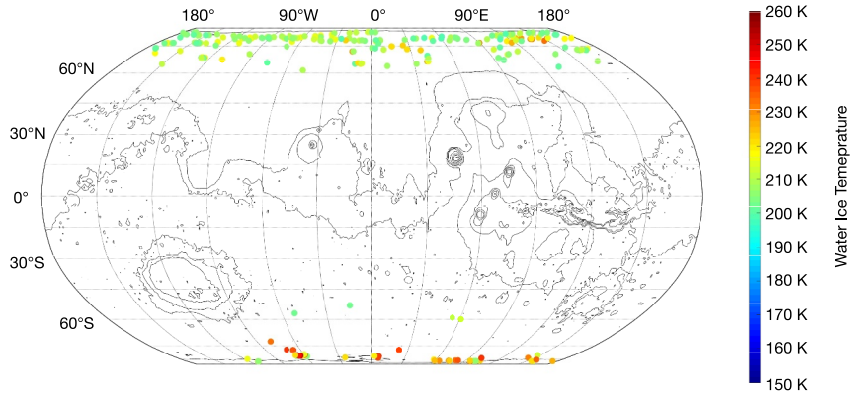

Figure 11. Distribution of the warm water frost (Temperature above $T_{E,\ Ca(ClO_4)_2} = 198$ K) detected with THEMIS on a Robinson projection map. Background contour lines are from MOLA topography (Zuber et al., 1992).

data from Khuller, Christensen, Harrison, and Diniega (2021)) who derived near-surface water vapor content from TES data assuming a well-mixed, hydrostatic, and isothermal atmosphere up to the H_2O condensation level (as done in Schorghofer & Aharonson, 2005). Values obtained are presented in Figure 12b. With this approach, the average surface water vapor for the Northern Hemisphere is 0.17 and 0.09 Pa for the South (Schorghofer & Aharonson, 2005). In comparison, the mean water vapor pressure derived from THEMIS temperature measurements is 0.12 Pa in the North and 0.0057 Pa in the South. Again, these measurements might be lower because of their time of acquisition (early morning/late afternoon) in comparison with the time of TES measurements (2 p.m., when the atmospheric water content is at maximum). Yet, the seasonal evolution of water vapor between TES and THEMIS is consistent: the maximum amount of water vapor is at the poles during the summer, and the atmosphere surrounding the seasonal CO_2 ice cap is dry. For very specific locations (for example, above 70°N, $80° \leq L_s \leq 110°$, THEMIS measurements show that the near-surface is enriched with water vapor. Indeed, at this time of the year, the sublimation of massive water ice deposits at the surface is supplying the dry atmosphere with water vapor. However, the sparse number of such defections prevents any generalization on a near-surface enrichment of water vapor.

We also present for completeness the comparison between THEMIS and Phoenix humidity measurements (Fischer et al., 2019) in Figure 13. As THEMIS does not specifically cover the Phoenix site (68.2°N, 234.3°E), we compare their measurements with those taken by THEMIS between 65°N and 75°N, without any longitude filter, assuming that it is representative of the Phoenix site. As THEMIS acquisitions were made between 6 and 8 a.m. and 6 and 8 p.m., we have isolated these data in the Phoenix data set. Both data sets mostly overlap during the second half of the Phoenix mission, between $L_s = 125°$ and $L_s = 145°$. In both cases, water vapor measurements are consistent, with values between 0.1 and 0.3 Pa, suggesting that our vapor pressure measurements are reliable. However, observational limitations (not always the same site observed, measurements procured at particular local times only when frost is present), prevent us from extending the intercomparison.

4. Discussion

4.1. Perennial Versus Seasonal Versus Diurnal Water Ice

Water ice deposits detected in this study could be either perennial, seasonal, or diurnal ice. Frosts detected at high latitudes during summer in the North are always found where massive ice deposits are observed and are thus considered perennial deposits (e.g., Figures 2a and 2b). At lower latitudes, frosts detected with THEMIS can be either diurnal or seasonal.

During the night, as the surface cools, a thin layer of water frost can form, which then sublimes during the morning. Phoenix's in-situ imagery revealed such diurnal frost (estimated to be a few micrometers thick, according to our model), even though the ice signature on the surface was very weak (see Figure 3b of P. H. Smith et al., 2009). Svitek and Murray (1990) have also detected diurnal water frost during spring at the Viking 2 landing site, noting that the brighter areas were linked to the thickest frosts. Finally, Landis (2007) detected frost at the Opportunity rover landing sites, but it was located on the deck of the rover and not on the surface. On the other

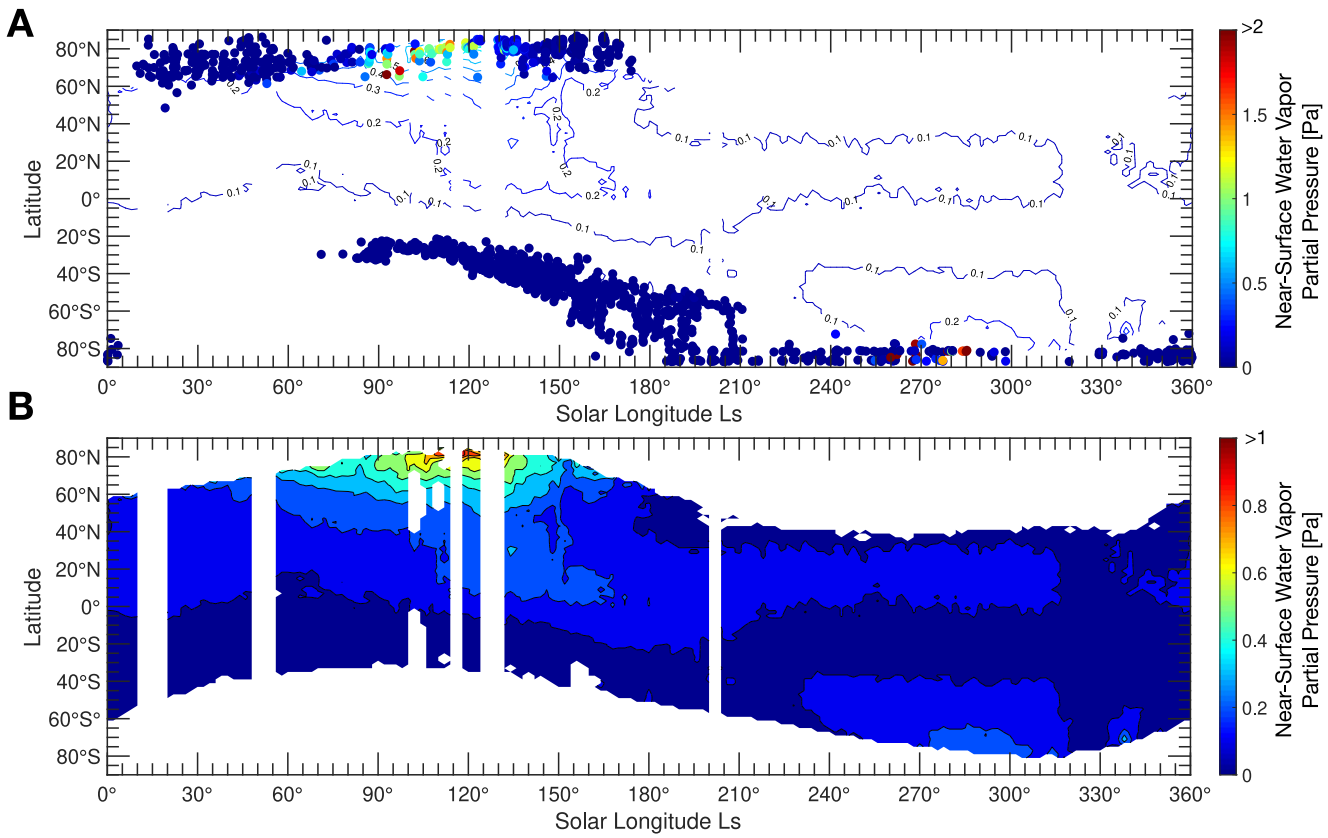

Figure 12. (a) Water vapor pressure derived from ice temperature measurements with THEMIS. Background colored contours are near-surface water vapor derived from TES measurements presented in panel (b). The color of the contours in panel (a) follows the color bar from panel (b).

hand, at the Curiosity landing site (4.5°S), diurnal water frost was assumed to be present given the environmental conditions of temperature and water vapor (Martínez et al., 2016) but was not formally detected with cameras and spectrometers (Schröder et al., 2015).

The Mars PCM predicts the formation of this diurnal frost during the night, quickly disappearing in the early morning (Figure 14a) during most of the year. For mid-to-high latitudes (above ±45° latitude), the diurnal thickness of water frost is at a maximum $\sim 2-10$ μm during the early spring and late autumn while being 1–2 μm thick during summer. At low latitudes (±30° latitude), frost thickness is at a maximum during northern summer, when the atmosphere is enriched in H_2O due to the sublimation of the northern perennial water ice cap (Smith, 2002) but is no thicker than 1–2 μm (Figure 14b). The diurnal water frost thickness during northern summer (L_s = 120°) predicted by the PCM between latitude 30°N and 30°S is shown in Figure 14c. In comparison, diurnal CO_2 frost is expected to be 10–100 μm thick, that is, 10 times larger than water ice (Piqueux et al., 2016). We acknowledge that the H_2O frost thicknesses computed by the PCM are upper limit since the model does not account for adsorption/desorption and exchange with the regolith. As shown by Jakosky et al. (1997); Steele et al. (2017) and Savijärvi et al. (2018), adsorption during the late afternoon should deplete the near-surface water vapor content, reducing the thickness of frost formed at night to less than one μm.

Could THEMIS detect such diurnal frost from orbit? It seems very unlikely for two reasons. First, our method mostly detects thick frosts, at least 100 μm thick (Figure 6, Section 3.1.1), that is, 10 times more thick than what is predicted for diurnal water frost. Therefore, it is improbable that such frost produces an albedo contrast with the bare surface strong enough to be detected with our method. Second, almost all of the frosts we have detected outside the poles are located within the stability domain of seasonal frost (Figure 7) and not outside of it, suggesting again that they are seasonal rather than diurnal. Hence, although the frosts detected in this study are mostly observed during the early morning and might at first glance be considered diurnal frosts, we conclude that they are actually seasonal frosts.

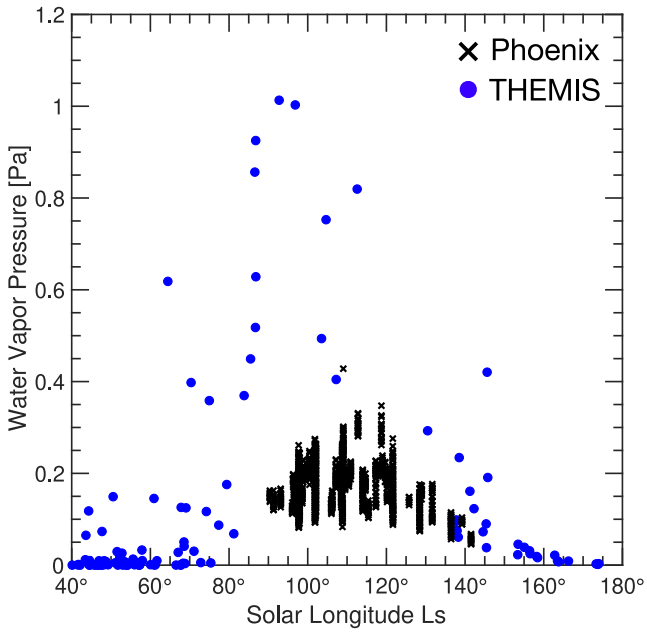

Figure 13. Water vapor pressure measured by Phoenix, using the calibration from Fischer et al. (2019), at 6–8 a.m. and 6–8 p.m. (dark crosses) and water vapor pressure derived from ice temperatures measured with THEMIS between 65°N and 75°N (blue points).

One area of interest to detect diurnal frost with THEMIS would be at the top of volcanoes, where the contrast between atmospheric and surface temperatures is strong (Fan et al., 2023), potentially creating a significant amount of frost every night (e.g., Figure 14). We have looked at the calderas of volcanoes in the ±40° latitude band and were unable to find any clear evidence of frost deposits. Indeed, the main bluish patterns we observed did not seem to correlate with the topography and could correspond either to surface-fogs, or clouds in the atmosphere (e.g., Inada et al., 2007; McConnochie et al., 2010). Valantinas et al. (2024) were able to demonstrate the presence of diurnal water frost on the caldera floor and rim of the Tharsis volcanoes with the Color and Stereo Surface Imaging System and High-Resolution Stereo Camera.

4.2. On the Existence of a Water Annulus in the South

The presence of H_2O ice deposits close to the CO_2 ice cap edge (Figures 7 and 9) can be explained by either small impurities of H_2O ice within the CO_2 ice cap, left as a lag when the CO_2 sublimes or a water ice annulus created by the sublimation-recondensation process proposed by Houben et al. (1997). The latter has been widely observed in the North (Appéré et al., 2011; Bibring et al., 2006; Kieffer & Titus, 2001; Wagstaff et al., 2008). In the South, its existence is less certain. Titus (2005) proposed the detection of an annulus at 85°S, and Bapst et al. (2015) suggested, using TES data, the existence of an annulus in the Southern Hemisphere during spring at 45–60°S. However, Bapst et al. (2015) acknowledged that their detection of a bright annulus might be due to the interpolation of their data or sub-grid pixel mixing and that high-resolution thermal and visible data were needed to conclude the existence of such annulus. Langevin et al. (2007), using OMEGA, did not observe large-scale expanses of water frost at the edge of the CO_2 cap but rather local signatures of water ice in the seasonal cap, considered as impurities. The few signatures of H_2O ice detected with OMEGA in the Southern Hemisphere at $L_s \leq 190°$ have either been interpreted as clouds or as frost confined in the South of Hellas (Langevin et al., 2007).

To test the existence of such an annulus, we have isolated the 441 detections made in the Southern Hemisphere during the receding phase of the seasonal CO_2 cap, that is, at latitudes ≤50°S and $90° \leq L_s \leq 270°$, and discriminate the nature of these deposits between H_2O ice impurities within the CO_2 cap and bright deposits close to the seasonal cap that could be interpreted as an annulus. Among these 441 water ice detections, 230 were made uniquely on pole-facing slopes and not on flat terrains, more than 1–2° latitude from the CO_2 ice cap. 112 detections show isolated water ice pixels within the CO_2 cap, which can either be attributed to impurities or have been detected on equatorward-facing slopes where CO_2 ice is barely stable. Other detections are large expanses of water ice (≥0.2° of latitudinal extent) close to the CO_2 cap, which could be interpreted as an annulus or frost deposits (e.g., Figures 2g and 2h). For each of these frost deposits, we measured their extent and reported them in Figure 15.

Contrary to Langevin et al. (2007), and in agreement with Bapst et al. (2015), we detect water ice during the first part of the sublimation of the seasonal cap ($L_s \leq 190°$) (e.g., Figures 2c and 2d). These ice deposits have a small extent, on average $0.9^{+1.3}_{-0.9}°$ at 1-σ of latitude, whereas the Northern annulus has an extent ranging from 5 to 10° (Appéré et al., 2011; Bibring et al., 2006; Kieffer & Titus, 2001; Wagstaff et al., 2008). This asymmetry is mostly explained by the asymmetry in atmospheric humidity between the two hemispheres. During winter and early spring, water ice is protected from sublimation by the cold trap formed by CO_2 ice. When the CO_2 ice disappears, the water ice is subjected to violent heating (Costard et al., 2002; Schorghofer, 2020), which causes it to disappear very quickly in a dry atmosphere, preventing the establishment of an extensive, stable annulus over time in the South. In comparison, in the North, the higher humidity stabilizes frost at the surface, preventing its rapid disappearance.

Can we confidently claim the existence of an annulus in the Southern Hemisphere? Water ices detected at the edge of the cap have an average temperature of 158.8 ± 4.8 K, that is, around 10 K higher than the condensation

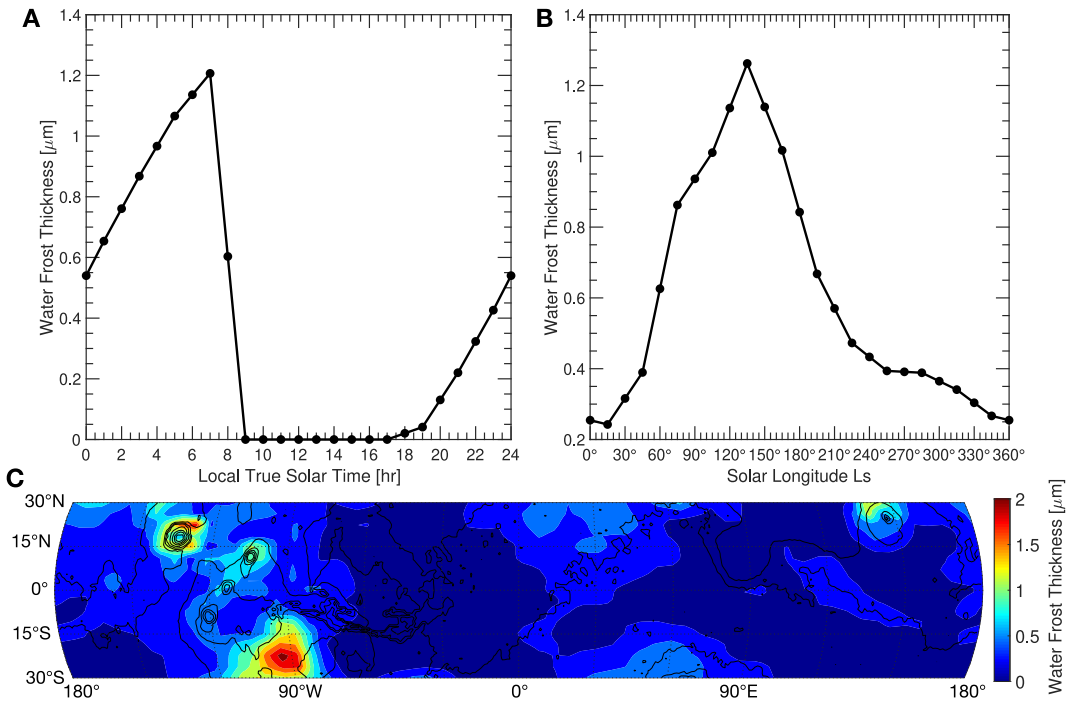

Figure 14. (a) Evolution of H_2O frost thickness predicted by the PCM at 15°N, 225°E, at L_s = 120° through the day. Dots represent the outputs from the PCM, which have been linearly interpolated (plain curve). (b) Evolution of H_2O frost thickness predicted by the PCM at 6 a.m., at 15°N, 225°E. (c) Map of the H_2O frost thickness predicted by the PCM at 6 a.m., L_s = 120° between 30°S and 30°N on a Robinson projection map. Background contour lines are from MOLA topography (Zuber et al., 1992). For the computations of the frost thicknesses, the local slope in the PCM grid (1° of resolution in latitude-longitude) is computed with MOLA data.

temperature of CO_2. But, as noted by Wagstaff et al. (2008), THEMIS observations at high latitudes can lead to measured CO_2 temperatures of more than 170 K. As stated in Section 2.2, we have manually eliminated these images and kept only those whose temperature is of the order of $T_{CO_2} \pm 5$ K where CO_2 is expected according to other observations (e.g., Piqueux et al., 2015) or the PCM. However, it still appears that the thermal contrast between CO_2 and H_2O ice is not as strong as that measured by Wagstaff et al. (2008) (around 20–30 K). It is therefore possible that the low-temperature water ice is actually CO_2 frost. Thus, we cannot conclude whether an annulus of water ice exists in the Southern Hemisphere during spring.

4.3. The Effect of Latent Heat on Ice Melting/Brine Formation

Section 3.2 has shown that neither ice temperatures measured by THEMIS, nor modeled by the PCM reach the melting point of 273.15 K. Ingersoll (1970) has shown that the cooling induced by the sublimation of ice was strong enough on Mars to prevent melting. His computations were updated by Schorghofer (2020), who also showed that ice temperature never reached 273.15 K. In both of their models, the sublimation is only driven by the gradient of density between the CO_2 atmosphere and the lighter H_2O vapor at the surface, with an isothermal atmosphere. However, as stated in Section 2.3.1, the sublimation of water ice is strongly dependent on (a) near-surface atmospheric stability, (b) gustiness induced by buoyant plumes, and (c) moisture roughness length. The state-of-the-art model by Khuller and Clow (2024), validated in a wide range of atmospheric conditions, shows that the sublimation of water ice at ∼273 K, with typical Martian atmospheric conditions, induces a significant latent heat flux, ∼1000 W m^{-2}, that is, almost two times the solar energy input. Hence, pure water ice cannot melt on present-day Mars. On the other hand, Clow (1987) and Williams et al. (2008) have shown that taking into account the heating of dust within the water ice by solar radiation (i.e., dirty snowpack model), a solid-state greenhouse effect occurs, which can lead to ice melting.

While the release of latent heat prevents pure ice from melting, it should not prevent the melting of ice contaminated by salts. Indeed, at the eutectic temperatures of Ca-perchlorate ($T_{E,\ Ca(ClO_4)_2} = 198$ K), Mg-chlorate

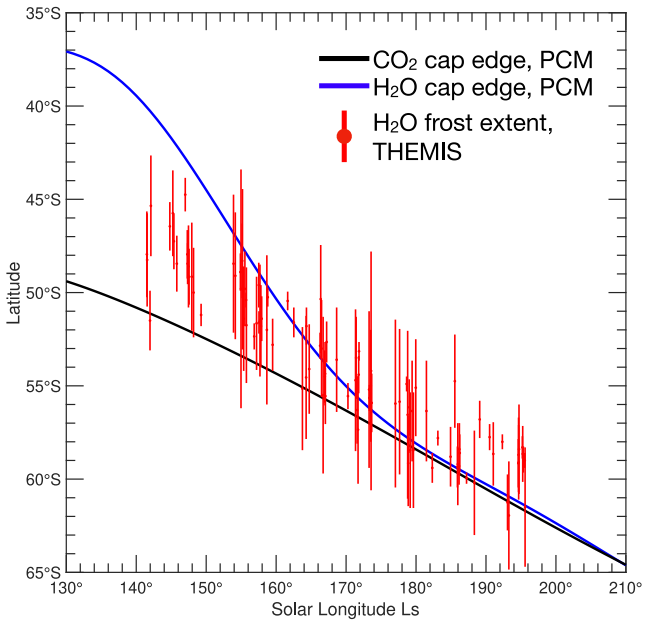

Figure 15. Latitudinal extent of H_2O frost deposits (red bar) during the recession of the seasonal CO_2 ice cap. The red bar represents the extent of H_2O frost, and the dots indicate their median latitudes. Plain curves represent the predicted stability of CO_2 (dark) and H_2O (blue) ice on a flat terrain by the PCM.

($T_{E,\ Mg(ClO_3)_2} = 206$ K), Mg-perchlorate ($T_{E,\ Mg(ClO_4)_2} = 212$ K), the latent heat flux associated with the sublimation of water ice is lower than 1 W m^{-2} (Khuller & Clow, 2024), and has a minimal impact on ice temperature. Hence, for these low temperatures, latent heat flux could not cool enough the ice to prevent the formation of brines. In this case, the limiting factor is not latent heat, but the quantity of water frost formed: as frost is only a few mm thick, it sublimates rapidly (in a few tens of sols), and can therefore disappear before it has time to reach these eutectic temperatures. However, the temperatures measured by THEMIS and modeled show that these temperatures can be reached (Figure 10). Na-perchlorate eutectic temperatures are very unlikely to be reached (Figure 10) as frost should sublimate before reaching this temperature, and latent heat effect should be stronger and cool the ice temperature (Khuller & Clow, 2024). Hence, we conclude that the more likely brine to form on Mars, based on temperature arguments, should be Ca-perchlorate, Mg-chlorate, and Mg-perchlorate rather than Na-perchlorate.

4.4. Effect of Frost on Subsurface Ice Stability

Massive quantities of ice have been discovered at high latitudes (above 55° of latitude) by the Mars Odyssey Neutron Spectrometer neutron spectrometers (Boynton et al., 2002; Diez et al., 2008; Feldman et al., 2002). The widely accepted theory to explain their geographical distribution and depth is that this ice is in equilibrium with near-surface water vapor (Mellon et al., 2004; Mellon & Jakosky, 1993; Schorghofer & Aharonson, 2005). Following their approach, subsurface ice is stable at a depth z if:

$$\overline{\left(\frac{p_{vap,surf}}{T_{surf}}\right)} \geq \overline{\left(\frac{p_{sv}(T_{soil}(z))}{T_{soil}(z)}\right)} \tag{9}$$

where overbars indicate time-averages over a complete MY, $p_{vap,surf}$ (Pa) is the vapor pressure at the surface, T_{surf} (K), is the surface temperature, $p_{sv,soil}$ (Pa) is the saturation vapor pressure that is a function of the soil temperature T_{soil} (K) (Murphy & Koop, 2005). During the night and during winter, the surface is saturated. To account for this effect, Mellon et al. (2004) and Schorghofer and Aharonson (2005) compute $p_{vap,surf}$ as:

$$p_{vap,surf} = \min\left(p_{vap,near-surface},\ p_{sv,surf}(T_{surf})\right) \tag{10}$$

where $p_{vap,near-surface}$ (Pa) is the near-surface water vapor content in the atmosphere, derived from observations or models.

However, the discovery of mid-latitude ice via ice-excavating impact craters (Byrne et al., 2009; Dundas et al., 2023; Dundas, Mellon, et al., 2021) has shown that the water vapor exchange theory does not explain the presence of this ice so low in latitude with the current atmospheric humidity. Models need to double/triple the humidity to explain the stability of subsurface ice at such low latitudes (Lange, Forget, Vincendon, et al., 2023; Mellon et al., 2004), suggesting that models are either underestimating near-surface humidity or that this ice is currently unstable, very slowly sublimating toward the equilibrium depth. The same problem arises for permafrost in Antarctica's dry valleys, where models predict a too-high sublimation rate of subsurface ice compared to observations (see a review in Fisher et al., 2016). Hagedorn et al. (2007) and McKay (2009) have shown that snow/frost on the surface could stabilize the subsurface ice in Antartica by reducing the humidity gradient between the surface and the ice table, inhibiting the sublimation loss from subsurface ice. Bapst et al. (2015) suggested that this effect might help solve the discrepancy in the distribution of subsurface ice between the models and the observations. In theory, the effect of surface frost is partially considered with Equation 10. However, this equation does not consider the case when a warm frost is sublimating, and one has: $p_{sv,surf}(T_{surf}) \geq p_{vap,near-surface}$, that is, when frost sublimation replenishes the atmosphere with water vapor (e.g., Section 3.3). In this case, Equation 10 underestimates the flux of water vapor coming from the surface. For an atmosphere with a water

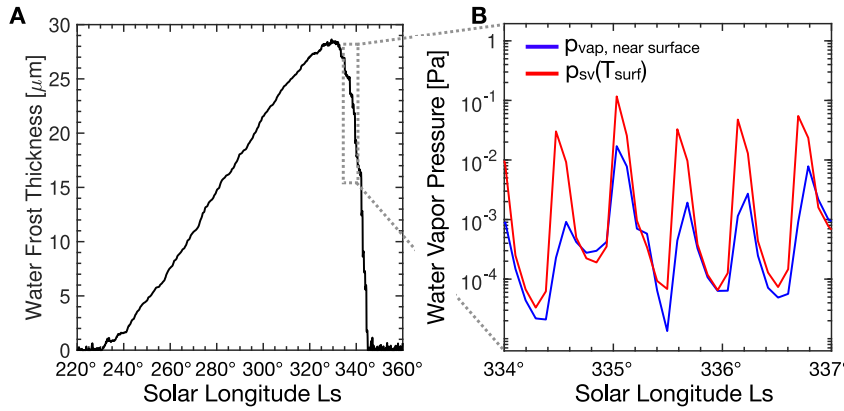

Figure 16. (a) Evolution of H_2O frost thickness predicted by the PCM at 52.5°N, 0°E (corresponding to a grid point where the PCM does not predict stable subsurface ice (Figure 3 of Lange, Forget, Vincendon, et al., 2023), while seasonal temperature variations show its presence in the first meter of the ground (Piqueux et al., 2019)) during the year. (b) Water vapor pressure predicted by the PCM (blue curve) in the first vertical layer (~4 m) and water vapor pressure at saturation over ice computed with Equation 1 (red curve) between $L_s = 334°$ and 337° (gray box in panel a) for the same location.

pressure of 0.2 Pa (typical of spring at mid-latitudes, Figure 12), this effect becomes apparent as soon as $T_{ice} \geq$ 200 K, a range of temperatures measured by THEMIS (Figure 10). PCM simulations show that this effect is mostly significant during the sublimation of seasonal/diurnal water ice (e.g., Figure 16) when warm frost acts as a significant source of water vapor in a dry atmosphere.

To quantify the effect of water frost on the yearly average near-surface water content, and therefore the stability of subsurface ice, we have changed the computation of the boundary condition given by Equation 10 with:

$$p_{\mathrm{vap,surf}} = \begin{cases} p_{\mathrm{vap,near-surface}} & \text{if frost thickness} > 10^{-7}\ \mathrm{m} \\ p_{\mathrm{sv,surf}}(T_{\mathrm{surf}}) & \text{if frost thickness} < 10^{-7}\ \mathrm{m} \end{cases} \quad (11)$$

We have chosen 10^{-7} m as the tolerance to avoid any effect of numerical noise. With this new boundary condition, we found that the mean annual humidity is higher by 20% between latitude 40°N and 60°N and similarly in the South, far from the +200% needed to model the same subsurface ice distribution as observed. In terms of depth, this means a change of mm/cm. This effect is thus not sufficient to explain the discrepancy between the ice-stability models based on Equation 9 and observations (Lange, Forget, Vincendon, et al., 2023). Furthermore, as warm frosts are found locally on slopes at mid-low latitudes, the effect of warm frost on the depth of the ice table would be local, and not regional/global.

Williams et al. (2015) have also studied the effect of surface frost on subsurface ice stability using a different approach. They have modeled the formation of subsurface ice solving the complete water vapor diffusion in the soil and found that frost has a significant impact on the depth of the stable ice table at the Viking 2 location (48°N). We cannot say whether the result comes directly from the effect of the frost on the surface or from their model. We are currently carrying out an intercomparison study between Equation 9–based models and full diffusion models to better understand this difference.

5. Conclusions

The objectives of this paper are to present new detections of water ice on Mars using THEMIS images, derive their temperature, and propose a unique data set of near-surface water vapor. The main conclusions of this investigation are:

1. Cross-analysis of the pixels that appear bright blue-white in visible THEMIS images with infrared temperature measurements allows us to determine whether the ice is composed of CO_2 or H_2O (Figure 2).
2. We detect water ice on 2,006 images, down to 21.4°S, 48.4°N, mostly on pole-facing slopes at low latitudes (lower than 45° latitude) and evenly on both flat and sloped terrains at higher latitudes (Figures 5, 7, and 9).

3. The evolution of water-ice deposits through the year at mid-latitude in the South is consistent with OMEGA/CRISM observations from Vincendon, Forget, and Mustard (2010) and the Mars PCM (Figure 8).
4. Like Vincendon, Forget, and Mustard (2010), and contrary to Bapst et al. (2015), we have been able to detect water ice in the Southern Hemisphere during autumn (Figure 8). Yet, these detections are only on pole-facing slopes at low latitudes, where Bapst et al. (2015) could not survey because of the resolution of TES.
5. The mean temperature of water ice measured by THEMIS is 170.9 ± 17 K at 1-σ, with a maximum value of 253.3 K, 10 K lower than the maximum frost temperature predicted by the PCM. 267 images show water frost warm enough to enable the formation of brines (Figures 10 and 11).
6. Near-surface vapor pressures derived from ice temperatures measured by THEMIS are lower than expected based on TES data, but this difference is mostly due to the difference in acquisition local times, thus biasing the comparison (Figure 12). A similar bias occurs when comparing THEMIS to Phoenix measurements (Figure 13).
7. Water ice frosts detected in this study are most likely related to seasonal ice rather than diurnal ice, which may be too thin to be detected (Figure 14).
8. We found water ice at the edge of the southern seasonal CO_2 ice cap during its recession. However, we cannot conclude whether there is or is not an annulus present given the small thermal contrast between water ice at the edges of the seasonal cap and the CO_2 ice cap itself (Figure 15).
9. Melting of pure water ice is impossible on present-day Mars because of the cooling induced by the latent heat (Ingersoll, 1970; Khuller & Clow, 2024; Schorghofer, 2020). However, this conclusion does not apply to dusty ice, where a solid-state greenhouse effect might enable melting (Clow, 1987; Williams et al., 2008). Brine formation is not limited by latent heat, but only by the thickness of the frost. If the frosts are too thin, they disappear before reaching eutectic temperatures. Thus, brine formation at low eutectic temperatures (Ca-perchlorate, Mg-chlorate, Mg-perchlorate) is more likely than at high eutectic temperatures (Na-perchlorate) (Section 4.3).
10. Diurnal and seasonal water frost help to stabilize the subsurface ice by reducing the humidity gradient and acting as a source of vapor when frost sublimes. Yet, this effect is not sufficient to explain the stability of subsurface ice at mid-latitudes as revealed by impact craters excavating ice (Figure 16).

To better constrain exchanges between the surface and the atmosphere, future work could leverage additional THEMIS bands to spectrally characterize the properties of these ices and constrain their dust content, as for instance performed with HiRISE data (Khuller & Christensen, 2021).

Data Availability Statement

The Mars PCM used in this work can be downloaded with documentation at https://svn.lmd.jussieu.fr/Planeto/trunk/LMDZ.MARS/. More information and documentation are available at http://www-planets.lmd.jussieu.fr. THEMIS visible and infrared images can be retrieved from the Planetary Data System (PDS) (P. Christensen, 2002; P. R. Christensen, 2002). MOLA topography map can be retrieved from the PDS (Smith et al., 1999). Data files for figures used in this analysis are available in a public repository, see Lange et al. (2024).

Acknowledgments
This project has received funding from the European Research Council under the European Union's Horizon 2020 research and innovation program (Grant 835275, project "Mars Through Time"). Mars PCM simulations were done thanks to the High-Performance Computing resources of Centre Informatique National de l'Enseignement Supérieur (CINES) under the allocation n°A0100110391 made by Grand Equipement National de Calcul Intensif (GENCI). Part of this work was performed at the Jet Propulsion Laboratory, California Institute of Technology under a contract with NASA (80NM0018-D0004). US Government support is acknowledged. The authors appreciate constructive comments and suggestions by D. Rogers and two anonymous reviewers which helped improve this manuscript.

References

Appéré, T., Schmitt, B., Langevin, Y., Douté, S., Pommerol, A., Forget, F., et al. (2011). Winter and spring evolution of northern seasonal deposits on Mars from OMEGA on Mars Express. *Journal of Geophysical Research*, *116*(E5), E05001. https://doi.org/10.1029/2010je003762

Bapst, J., Bandfield, J. L., & Wood, S. E. (2015). Hemispheric asymmetry in Martian seasonal surface water ice from MGS TES. *Icarus*, *260*, 396–408. https://doi.org/10.1016/j.icarus.2015.07.025

Bapst, J., Byrne, S., Bandfield, J. L., & Hayne, P. O. (2019). Thermophysical properties of the North polar residual cap using Mars global surveyor thermal emission spectrometer. *Journal of Geophysical Research: Planets*, *124*(5), 1315–1330. https://doi.org/10.1029/2018JE005786

Bennett, K. A., Hill, J. R., Murray, K. C., Edwards, C. S., Bell III, J. F., & Christensen, P. R. (2018). THEMIS-VIS investigations of sand at Gale crater. *Earth and Space Science*, *5*(8), 352–363. https://doi.org/10.1029/2018EA000380

Bibring, J.-P., Langevin, Y., Mustard, J. F., Poulet, F., Arvidson, R., Gendrin, A., et al. (2006). Global mineralogical and aqueous Mars history derived from OMEGA/Mars express data. *Science*, *312*(5772), 400–404. https://doi.org/10.1126/science.1122659

Boynton, W. V., Feldman, W. C., Squyres, S. W., Prettyman, T. H., Bruckner, J., Evans, L. G., et al. (2002). Distribution of hydrogen in the near surface of Mars: Evidence for subsurface ice deposits. *Science*, *297*(5578), 81–85. https://doi.org/10.1126/science.1073722

Bramson, A. M., Byrne, S., Bapst, J., Smith, I. B., & McClintock, T. (2019). A migration model for the polar spiral troughs of Mars. *Journal of Geophysical Research: Planets*, *124*(4), 1020–1043. https://doi.org/10.1029/2018je005806

Brutsaert, W. (1982). The lower atmosphere. In *Evaporation into the atmosphere: Theory, history and applications* (pp. 37–56). Springer. https://doi.org/10.1007/978-94-017-1497-6_3

Byrne, S., Dundas, C. M., Kennedy, M. R., Mellon, M. T., McEwen, A. S., Cull, S. C., et al. (2009). Distribution of mid-latitude ground ice on Mars from new impact craters. *Science*, *325*(5948), 1674–1676. https://doi.org/10.1126/science.1175307

Calvin, W., James, P., Cantor, B., & Dixon, E. (2015). Interannual and seasonal changes in the north polar ice deposits of Mars: Observations from MY 29–31 using MARCI. *Icarus*, *251*, 181–190. (Dynamic Mars). https://doi.org/10.1016/j.icarus.2014.08.026

Carrozzo, F. G., Bellucci, G., Altieri, F., D'Aversa, E., & Bibring, J. P. (2009). Mapping of water frost and ice at low latitudes on Mars. *Icarus*, *203*(2), 406–420. https://doi.org/10.1016/j.icarus.2009.05.020

Chevrier, V. F., Fitting, A. B., & Rivera-Valentín, E. G. (2022). Limited stability of multicomponent brines on the surface of Mars. *The Planetary Science Journal*, *3*(5), 125. https://doi.org/10.3847/psj/ac6603

Christensen, P. (2002). Odyssey THEMIS-VIS geo v2.0 [Dataset]. *NASA Planetary Data System*. https://doi.org/10.17189/1520386

Christensen, P. R. (2002). Odyssey THEMIS IR PBT V2.0 [Dataset]. *NASA Planetary Data System*. https://doi.org/10.17189/1520354

Christensen, P. R., Bandfield, J. L., Hamilton, V. E., Ruff, S. W., Kieffer, H. H., Titus, T. N., et al. (2001). Mars global surveyor thermal emission spectrometer experiment: Investigation description and surface science results. *Journal of Geophysical Research*, *106*(E10), 23823–23871. https://doi.org/10.1029/2000je001370

Christensen, P. R., Jakosky, B. M., Kieffer, H. H., Malin, M. C., Harry, Y., McSween, J., et al. (2004). The thermal emission imaging System (THEMIS) for the Mars 2001 Odyssey mission. *Space Science Reviews*, *110*(1/2), 85–130. https://doi.org/10.1023/b:spac.0000021008.16305.94

Clark, B. (1981). The salts of Mars. *Icarus*, *45*(2), 370–378. https://doi.org/10.1016/0019-1035(81)90041-5

Clow, G. D. (1987). Generation of liquid water on Mars through the melting of a dusty snowpack. *Icarus*, *72*(1), 95–127. https://doi.org/10.1016/0019-1035(87)90123-0

Colaïtis, A., Spiga, A., Hourdin, F., Rio, C., Forget, F., & Millour, E. (2013). A thermal plume model for the Martian convective boundary layer. *Journal of Geophysical Research: Planets*, *118*(7), 1468–1487. https://doi.org/10.1002/jgre.20104

Costard, F., Forget, F., Mangold, N., & Peulvast, J. P. (2002). Formation of recent Martian debris flows by melting of near-surface ground ice at high obliquity. *Science*, *295*(5552), 110–113. https://doi.org/10.1126/science.1066698

Curran, R. J., Conrath, B. J., Hanel, R. A., Kunde, V. G., & Pearl, J. C. (1973). Mars: Mariner 9 spectroscopic evidence for H_2O ice clouds. *Science*, *182*(4110), 381–383. https://doi.org/10.1126/science.182.4110.381

Diez, B., Feldman, W., Maurice, S., Gasnault, O., Prettyman, T., Mellon, M., et al. (2008). H layering in the top meter of Mars. *Icarus*, *196*(2), 409–421. https://doi.org/10.1016/j.icarus.2008.02.006

Diniega, S., Bramson, A. M., Buratti, B., Buhler, P., Burr, D. M., Chojnacki, M., et al. (2021). Modern Mars' geomorphological activity, driven by wind, frost, and gravity. *Geomorphology*, *380*, 107627. https://doi.org/10.1016/j.geomorph.2021.107627

Dundas, C. M., Becerra, P., Byrne, S., Chojnacki, M., Daubar, I. J., Diniega, S., et al. (2021). Active Mars: A dynamic world. *Journal of Geophysical Research: Planets*, *126*(8), e2021JE006876. https://doi.org/10.1029/2021JE006876

Dundas, C. M., & Byrne, S. (2010). Modeling sublimation of ice exposed by new impacts in the Martian mid-latitudes. *Icarus*, *206*(2), 716–728. https://doi.org/10.1016/j.icarus.2009.09.007

Dundas, C. M., McEwen, A. S., Diniega, S., Hansen, C. J., Byrne, S., & McElwaine, J. N. (2019). *The formation of gullies on Mars today* (Vol. 467, pp. 67–94). Geological Society of London Special Publications. https://doi.org/10.1144/SP467.5

Dundas, C. M., Mellon, M. T., Conway, S. J., Daubar, I. J., Williams, K. E., Ojha, L., et al. (2021). Widespread exposures of extensive clean shallow ice in the midlatitudes of Mars. *Journal of Geophysical Research: Planets*, *126*(3). https://doi.org/10.1029/2020je006617

Dundas, C. M., Mellon, M. T., Posiolova, L. V., Miljković, K., Collins, G. S., Tornabene, L. L., et al. (2023). A large new crater exposes the limits of water ice on Mars. *Geophysical Research Letters*, *50*(2), e2022GL100747. https://doi.org/10.1029/2022GL100747

England, D. E., & McNider, R. T. (1995). Stability functions based upon shear functions. *Boundary-Layer Meteorology*, *74*(1–2), 113–130. https://doi.org/10.1007/bf00715713

Fan, B., Jansen, M. F., Mischna, M. A., & Kite, E. S. (2023). Why are mountaintops cold? The transition of surface lapse rate on dry planets. *Geophysical Research Letters*, *50*(23). https://doi.org/10.1029/2023gl106683

Feldman, W. C., Boynton, W. V., Tokar, R. L., Prettyman, T. H., Gasnault, O., Squyres, S. W., et al. (2002). Global distribution of neutrons from Mars: Results from Mars Odyssey. *Science*, *297*(5578), 75–78. https://doi.org/10.1126/science.1073541

Fergason, R. L., Christensen, P. R., & Kieffer, H. H. (2006). High-resolution thermal inertia derived from the thermal emission imaging System (THEMIS): Thermal model and applications. *Journal of Geophysical Research*, *111*(E12). https://doi.org/10.1029/2006JE002735

Fischer, E., Martínez, G. M., Rennó, N. O., Tamppari, L. K., & Zent, A. P. (2019). Relative humidity on Mars: New results from the Phoenix TECP sensor. *Journal of Geophysical Research: Planets*, *124*(11), 2780–2792. https://doi.org/10.1029/2019JE006080

Fisher, D. A., Lacelle, D., Pollard, W., Davila, A., & McKay, C. P. (2016). Ground surface temperature and humidity, ground temperature cycles and the ice table depths in University Valley, McMurdo Dry Valleys of Antarctica. *Journal of Geophysical Research: Earth Surface*, *121*(11), 2069–2084. https://doi.org/10.1002/2016jf004054

Fitzpatrick, N., Radić, V., & Menounos, B. (2019). A multi-season investigation of glacier surface roughness lengths through in situ and remote observation. *The Cryosphere*, *13*(3), 1051–1071. https://doi.org/10.5194/tc-13-1051-2019

Flanner, M. G., Arnheim, J. B., Cook, J. M., Dang, C., He, C., Huang, X., et al. (2021). SNICAR-ADv3: A community tool for modeling spectral snow albedo. *Geoscientific Model Development*, *14*(12), 7673–7704. https://doi.org/10.5194/gmd-14-7673-2021

Flasar, F., & Goody, R. M. (1976). Diurnal behaviour of water on Mars. *Planetary and Space Science*, *24*(2), 161–181. https://doi.org/10.1016/0032-0633(76)90103-3

Foken, T. (2006). 50 years of the Monin–Obukhov similarity theory. *Boundary-Layer Meteorology*, *119*(3), 431–447. https://doi.org/10.1007/s10546-006-9048-6

Forget, F., Hourdin, F., Fournier, R., Hourdin, C., Talagrand, O., Collins, M., et al. (1999). Improved general circulation models of the Martian atmosphere from the surface to above 80 km. *Journal of Geophysical Research*, *104*(E10), 24155–24175. https://doi.org/10.1029/1999JE001025

Glavin, D. P., Freissinet, C., Miller, K. E., Eigenbrode, J. L., Brunner, A. E., Buch, A., et al. (2013). Evidence for perchlorates and the origin of chlorinated hydrocarbons detected by SAM at the Rocknest Aeolian deposit in Gale Crater. *Journal of Geophysical Research: Planets*, *118*(10), 1955–1973. https://doi.org/10.1002/jgre.20144

Haberle, R. M., Forget, F., Colaprete, A., Schaeffer, J., Boynton, W. V., Kelly, N. J., & Chamberlain, M. A. (2008). The effect of ground ice on the Martian seasonal CO_2 cycle. *Planetary and Space Science*, *56*(2), 251–255. https://doi.org/10.1016/j.pss.2007.08.006

Haberle, R. M., Kahre, M. A., Hollingsworth, J. L., Montmessin, F., Wilson, R. J., Urata, R. A., et al. (2019). Documentation of the NASA/Ames legacy Mars global climate model: Simulations of the present seasonal water cycle. *Icarus*, *333*, 130–164. https://doi.org/10.1016/j.icarus.2019.03.026

Hagedorn, B., Sletten, R. S., & Hallet, B. (2007). Sublimation and ice condensation in hyperarid soils: Modeling results using field data from Victoria Valley, Antarctica. *Journal of Geophysical Research*, *112*(F3). https://doi.org/10.1029/2006jf000580

Harri, A., Genzer, M., Kemppinen, O., Gomez-Elvira, J., Haberle, R., Polkko, J., et al. (2014). Mars Science Laboratory relative humidity observations: Initial results. *Journal of Geophysical Research: Planets*, *119*(9), 2132–2147. https://doi.org/10.1002/2013je004514

Hébrard, E., Listowski, C., Coll, P., Marticorena, B., Bergametti, G., Määttänen, A., et al. (2012). An aerodynamic roughness length map derived from extended Martian rock abundance data. *Journal of Geophysical Research (Planets)*, *117*(E4), E04008. https://doi.org/10.1029/2011JE003942

Hecht, M. H., Kounaves, S. P., Quinn, R. C., West, S. J., Young, S. M. M., Ming, D. W., et al. (2009). Detection of perchlorate and the soluble chemistry of Martian soil at the Phoenix lander site. *Science*, *325*(5936), 64–67. https://doi.org/10.1126/science.1172466

Hess, S. L. (1979). Static stability and thermal wind in an atmosphere of variable composition: Applications to Mars. *Journal of Geophysical Research*, *84*(B6), 2969–2973. https://doi.org/10.1029/jb084ib06p02969

Houben, H., Haberle, R. M., Young, R. E., & Zent, A. P. (1997). Modeling the Martian seasonal water cycle. *Journal of Geophysical Research*, *102*(E4), 9069–9083. https://doi.org/10.1029/97je00046

Inada, A., Richardson, M. I., McConnochie, T. H., Strausberg, M. J., Wang, H., & Bell, J. F. (2007). High-resolution atmospheric observations by the Mars Odyssey thermal emission imaging System. *Icarus*, *192*(2), 378–395. https://doi.org/10.1016/j.icarus.2007.07.020

Ingersoll, A. P. (1970). Mars: Occurrence of liquid water. *Science*, *168*(3934), 972–973. https://doi.org/10.1126/science.168.3934.972

Jakosky, B. M., Zent, A. P., & Zurek, R. W. (1997). The Mars water cycle: Determining the role of exchange with the regolith. *Icarus*, *130*(1), 87–95. https://doi.org/10.1006/icar.1997.5799

James, P. B., Briggs, G., Barnes, J., & Spruck, A. (1979). Seasonal recession of Mars' south polar cap as seen by Viking. *Journal of Geophysical Research*, *84*(B6), 2889–2922. https://doi.org/10.1029/jb084ib06p02889

James, P. B., Kieffer, H. H., & Paige, D. A. (1992). The seasonal cycle of carbon dioxide on Mars. In *Mars* (pp. 934–968). University of Arizona Press.

Jiménez, P. A., Dudhia, J., González-Rouco, J. F., Navarro, J., Montávez, J. P., & García-Bustamante, E. (2012). A revised scheme for the WRF surface layer formulation. *Monthly Weather Review*, *140*(3), 898–918. https://doi.org/10.1175/mwr-d-11-00056.1

Joshi, M. M., Lewis, S. R., Read, P. L., & Catling, D. C. (1994). Western boundary currents in the atmosphere of Mars. *Nature*, *367*(6463), 548–551. https://doi.org/10.1038/367548a0

Joshi, M. M., Lewis, S. R., Read, P. L., & Catling, D. C. (1995). Western boundary currents in the Martian atmosphere: Numerical simulations and observational evidence. *Journal of Geophysical Research*, *100*(E3), 5485–5500. https://doi.org/10.1029/94JE02716

Kahre, M., Haberle, R., Hollingsworth, J., & Wolff, M. (2020). MARCI-observed clouds in the Hellas basin during northern hemisphere summer on Mars: Interpretation with the NASA/Ames legacy Mars global climate model. *Icarus*, *338*, 113512. https://doi.org/10.1016/j.icarus.2019.113512

Kereszturi, A., Möhlmann, D., Berczi, S., Ganti, T., Horvath, A., Kuti, A., et al. (2010). Indications of brine related local seepage phenomena on the northern hemisphere of Mars. *Icarus*, *207*(1), 149–164. https://doi.org/10.1016/j.icarus.2009.10.012

Kereszturi, A., Vincendon, M., & Schmidt, F. (2011). Water ice in the dark dune spots of Richardson crater on Mars. *Planetary and Space Science*, *59*(1), 26–42. https://doi.org/10.1016/j.pss.2010.10.015

Khuller, A. R., & Christensen, P. R. (2021). Evidence of exposed dusty water ice within Martian Gullies. *Journal of Geophysical Research: Planets*, *126*(2). https://doi.org/10.1029/2020je006539

Khuller, A. R., Christensen, P. R., Harrison, T. N., & Diniega, S. (2021). The distribution of frosts on Mars: Links to present-day gully activity. *Journal of Geophysical Research: Planets*, *126*(3), e2020JE006577. https://doi.org/10.1029/2020JE006577

Khuller, A. R., Christensen, P. R., & Warren, S. G. (2021). Spectral albedo of dusty Martian H_2O snow and ice. *Journal of Geophysical Research: Planets*, *126*(9), e2021JE006910. https://doi.org/10.1029/2021JE006910

Khuller, A. R., & Clow, G. D. (2024). Turbulent fluxes and evaporation/sublimation rates on Earth, Mars, Titan, and Exoplanets. *Journal of Geophysical Research: Planets*, *129*(4), e2023JE008114. https://doi.org/10.1029/2023JE008114

Kieffer, H. H. (2013). Thermal model for analysis of Mars infrared mapping. *Journal of Geophysical Research: Planets*, *118*(3), 451–470. https://doi.org/10.1029/2012JE004164

Kieffer, H. H., & Titus, T. N. (2001). TES mapping of Mars' north seasonal cap. *Icarus*, *154*(1), 162–180. https://doi.org/10.1006/icar.2001.6670

Kite, E. S., Halevy, I., Kahre, M. A., Wolff, M. J., & Manga, M. (2013). Seasonal melting and the formation of sedimentary rocks on Mars, with predictions for the Gale Crater mound. *Icarus*, *223*(1), 181–210. https://doi.org/10.1016/j.icarus.2012.11.034

Landis, G. A. (2007). Observation of frost at the equator of Mars by the opportunity rover. (The Lunar and Planetary Science Conference) https://www.lpi.usra.edu/meetings/lpsc2007/pdf/2423.pdf

Lange, L., Forget, F., Dupont, E., Vandemeulebrouck, R., Spiga, A., Millour, E., et al. (2023). Modeling slope microclimates in the Mars planetary climate model. *Journal of Geophysical Research: Planets*, *128*(10), e2023JE007915. https://doi.org/10.1029/2023JE007915

Lange, L., Forget, F., Vincendon, M., Spiga, A., Vos, E., Aharonson, O., et al. (2023). A reappraisal of subtropical subsurface water ice stability on Mars. *Geophysical Research Letters*, *50*(21), e2023GL105177. https://doi.org/10.1029/2023GL105177

Lange, L., Piqueux, S., Edwards, C., Forget, F., Naar, J., Vos, E., & Szantai, A. (2024). Replication data for: Observations of water frost on Mars with THEMIS: Application to the presence of brines and the stability of (Sub)Surface water ice, V2 [Dataset]. *Harvard Dataverse*. https://doi.org/10.7910/DVN/3OMRM2

Lange, L., Piqueux, S., & Edwards, C. S. (2022). Gardening of the Martian regolith by diurnal CO_2 frost and the formation of slope streaks. *Journal of Geophysical Research: Planets*, *127*(4), e2021JE006988. https://doi.org/10.1029/2021JE006988

Langevin, Y., Bibring, J.-P., Montmessin, F., Forget, F., Vincendon, M., Douté, S., et al. (2007). Observations of the south seasonal cap of Mars during recession in 2004–2006 by the OMEGA visible/near-infrared imaging spectrometer on board Mars express. *Journal of Geophysical Research*, *112*(E8), E08S12. https://doi.org/10.1029/2006JE002841

Larsen, S. E., Jørgensen, H. E., Landberg, L., & Tillman, J. E. (2002). Aspects of the atmospheric surface layers on Mars and Earth. *Boundary-Layer Meteorology*, *105*(3), 451–470. https://doi.org/10.1023/a:1020338016753

Leighton, R. B., & Murray, B. C. (1966). Behavior of carbon dioxide and other volatiles on Mars. *Science*, *153*(3732), 136–144. https://doi.org/10.1126/science.153.3732.136

Leung, C. W., Tamppari, L. K., Kass, D. M., Martínez, G., Fischer, E., & Smith, M. D. (2024). Seasonal vertical water vapor distribution at the Mars Phoenix Lander site. *Icarus*, *408*, 115820. https://doi.org/10.1016/j.icarus.2023.115820

Madeleine, J.-B., Forget, F., Millour, E., Navarro, T., & Spiga, A. (2012). The influence of radiatively active water ice clouds on the Martian climate. *Geophysical Research Letters*, *39*(23). https://doi.org/10.1029/2012gl053564

Malin, M. C., Bell III, J. F., Cantor, B. A., Caplinger, M. A., Calvin, W. M., Clancy, R. T., et al. (2007). Context camera investigation on board the Mars reconnaissance orbiter. *Journal of Geophysical Research*, *112*(E5). https://doi.org/10.1029/2006JE002808

Martin, L. J., & Zurek, R. W. (1993). An analysis of the history of dust activity on Mars. *Journal of Geophysical Research*, *98*(E2), 3221–3246. https://doi.org/10.1029/92je02937

Martínez, G., Fischer, E., Rennó, N., Sebastián, E., Kemppinen, O., Bridges, N., et al. (2016). Likely frost events at Gale crater: Analysis from MSL/REMS measurements. *Icarus*, *280*, 93–102. (MicroMars to MegaMars). https://doi.org/10.1016/j.icarus.2015.12.004

Martínez, G., Valero, F., & Vázquez, L. (2009). Characterization of the Martian surface layer. *Journal of the Atmospheric Sciences*, *66*(1), 187–198. https://doi.org/10.1175/2008jas2765.1

Martínez, G. M., Newman, C. N., De Vicente-Retortillo, A., Fischer, E., Renno, N. O., Richardson, M. I., et al. (2017). The modern near-surface Martian climate: A review of in-situ meteorological data from Viking to curiosity. *Space Science Reviews*, *212*(1–2), 295–338. https://doi.org/10.1007/s11214-017-0360-x

McConnochie, T. H., Bell, J. F., Savransky, D., Wolff, M. J., Toigo, A. D., Wang, H., et al. (2010). THEMIS-VIS observations of clouds in the Martian mesosphere: Altitudes, wind speeds, and decameter-scale morphology. *Icarus*, *210*(2), 545–565. https://doi.org/10.1016/j.icarus.2010.07.021

McEwen, A. S., Hansen, C. J., Delamere, W. A., Eliason, E. M., Herkenhoff, K. E., Keszthelyi, L., et al. (2007). A closer look at water-related geologic activity on Mars. *Science*, *317*(5845), 1706–1709. https://doi.org/10.1126/science.1143987

McKay, C. P. (2009). Snow recurrence sets the depth of dry permafrost at high elevations in the McMurdo Dry Valleys of Antarctica. *Antarctic Science*, *21*(1), 89–94. https://doi.org/10.1017/s0954102008001508

Mellon, M. T., Feldman, W. C., & Prettyman, T. H. (2004). The presence and stability of ground ice in the southern hemisphere of Mars. *Icarus*, *169*(2), 324–340. https://doi.org/10.1016/j.icarus.2003.10.022

Mellon, M. T., & Jakosky, B. M. (1993). Geographic variations in the thermal and diffusive stability of ground ice on Mars. *Journal of Geophysical Research*, *98*(E2), 3345–3364. https://doi.org/10.1029/92je02355

Möhlmann, D., & Kereszturi, A. (2010). Viscous liquid film flow on dune slopes of Mars. *Icarus*, *207*(2), 654–658. https://doi.org/10.1016/j.icarus.2010.01.002

Montabone, L., Forget, F., Millour, E., Wilson, R., Lewis, S., Cantor, B., et al. (2015). Eight-year climatology of dust optical depth on Mars. *Icarus*, *251*, 65–95. (Dynamic Mars). https://doi.org/10.1016/j.icarus.2014.12.034

Montmessin, F., Forget, F., Rannou, P., Cabane, M., & Haberle, R. M. (2004). Origin and role of water ice clouds in the Martian water cycle as inferred from a general circulation model. *Journal of Geophysical Research*, *109*(E10). https://doi.org/10.1029/2004je002284

Montmessin, F., Smith, M. D., Langevin, Y., Mellon, M. T., & Fedorova, A. (2017). The water cycle. In R. M. Haberle, R. T. Clancy, F. Forget, M. D. Smith, & R. W. Zurek (Eds.), *Asteroids, comets, meteors - acm2017* (pp. 295–337). Cambridge University Press. https://doi.org/10.1017/9781139060172.011

Murchie, S. L., Bibring, J.-P., Arvidson, R. E., Bishop, J. L., Carter, J., Ehlmann, B. L., et al. (2019). Visible to short-wave infrared spectral analyses of Mars from orbit using CRISM and OMEGA. In *Remote compositional analysis: Techniques for understanding spectroscopy, mineralogy, and geochemistry of planetary surfaces* (pp. 453–483). Cambridge University Press. https://doi.org/10.1017/9781316888872.025

Murphy, D. M., & Koop, T. (2005). Review of the vapour pressures of ice and supercooled water for atmospheric applications. *Quarterly Journal of the Royal Meteorological Society*, *131*(608), 1539–1565. https://doi.org/10.1256/qj.04.94

Murray, K. C., Christensen, P. R., & Mehall, G. L. (2016). *THEMIS geometric processing user's guide*. NASA, Planetary Data System, ODY-M-THM-5-VISGEO-V2.0. Retrieved from https://static.mars.asu.edu/pds/ODTGEO_v2/document/geometry.pdf

Naar, J., Forget, F., Vals, M., Millour, E., Bierjon, A., González-Galindo, F., & Richard, B. (2021). Modeling the global water cycle on Mars with improved physical parametrization. In *European planetary science congress* (p. EPSC2021-559). https://doi.org/10.5194/epsc2021-559

Navarro, T., Madeleine, J.-B., Forget, F., Spiga, A., Millour, E., Montmessin, F., & Määttänen, A. (2014). Global climate modeling of the Martian water cycle with improved microphysics and radiatively active water ice clouds. *Journal of Geophysical Research: Planets*, *119*(7), 1479–1495. https://doi.org/10.1002/2013JE004550

Osterloo, M. M., Anderson, F. S., Hamilton, V. E., & Hynek, B. M. (2010). Geologic context of proposed chloride-bearing materials on Mars. *Journal of Geophysical Research*, *115*(E10). https://doi.org/10.1029/2010je003613

Osterloo, M. M., Hamilton, V. E., Bandfield, J. L., Glotch, T. D., Baldridge, A. M., Christensen, P. R., et al. (2008). Chloride-Bearing materials in the southern highlands of Mars. *Science*, *319*(5870), 1651–1654. https://doi.org/10.1126/science.1150690

Pál, B., Kereszturi, Á., Forget, F., & Smith, M. D. (2019). Global seasonal variations of the near-surface relative humidity levels on present-day Mars. *Icarus*, *333*, 481–495. https://doi.org/10.1016/j.icarus.2019.07.007

Pilorget, C., Edwards, C. S., Ehlmann, B. L., Forget, F., & Millour, E. (2013). Material ejection by the cold jets and temperature evolution of the south seasonal polar cap of Mars from THEMIS/CRISM observations and implications for surface properties. *Journal of Geophysical Research (Planets)*, *118*(12), 2520–2536. https://doi.org/10.1002/2013je004513

Piqueux, S., Buz, J., Edwards, C. S., Bandfield, J. L., Kleinböhl, A., Kass, D. M., & Hayne, P. O. (2019). Widespread shallow water ice on Mars at high latitudesand midlatitudes. *Geophysical Research Letters*, *46*(24), 14290–14298. https://doi.org/10.1029/2019gl083947

Piqueux, S., Edwards, C. S., & Christensen, P. R. (2008). Distribution of the ices exposed near the south pole of Mars using Thermal Emission Imaging System (THEMIS) temperature measurements. *Journal of Geophysical Research*, *113*(E8). https://doi.org/10.1029/2007je003055

Piqueux, S., Kass, D. M., Kleinböhl, A., Slipski, M., Hayne, P. O., McCleese, D. J., et al. (2023). Mars thermal inertia and surface temperatures by the Mars Climate Sounder. *Icarus*, *115851*, 115851. https://doi.org/10.1016/j.icarus.2023.115851

Piqueux, S., Kleinböhl, A., Hayne, P. O., Heavens, N. G., Kass, D. M., McCleese, D. J., et al. (2016). Discovery of a widespread low-latitude diurnal CO2 frost cycle on Mars. *Journal of Geophysical Research: Planets*, *121*(7), 1174–1189. https://doi.org/10.1002/2016JE005034

Piqueux, S., Kleinböhl, A., Hayne, P. O., Kass, D. M., Schofield, J. T., & McCleese, D. J. (2015). Variability of the Martian seasonal CO_2 cap extent over eight Mars years. *Icarus*, *251*, 164–180. https://doi.org/10.1016/j.icarus.2014.10.045

Polkko, J., Hieta, M., Harri, A., Tamppari, L., Martínez, G., Viúdez-Moreiras, D., et al. (2023). Initial results of the relative humidity observations by MEDA instrument onboard the Mars 2020 perseverance rover. *Journal of Geophysical Research: Planets*, *128*(2). https://doi.org/10.1029/2022je007447

Pommerol, A., Thomas, N., Jost, B., Beck, P., Okubo, C., & McEwen, A. S. (2013). Photometric properties of Mars soils analogs. *Journal of Geophysical Research: Planets*, *118*(10), 2045–2072. https://doi.org/10.1002/jgre.20158

Putzig, N. E., Mellon, M. T., Kretke, K. A., & Arvidson, R. E. (2005). Global thermal inertia and surface properties of Mars from the MGS mapping mission. *Icarus*, *173*(2), 325–341. https://doi.org/10.1016/j.icarus.2004.08.017

Rivera-Valentín, E. G., Chevrier, V. F., Soto, A., & Martínez, G. (2020). Distribution and habitability of (meta)stable brines on present-day Mars. *Nature Astronomy*, *4*(8), 756–761. https://doi.org/10.1038/s41550-020-1080-9

Savijärvi, H. (1995). Mars boundary layer modeling: Diurnal moisture cycle and soil properties at the Viking Lander 1 site. *Icarus*, *117*(1), 120–127. https://doi.org/10.1006/icar.1995.1146

Savijärvi, H., Paton, M., & Harri, A.-M. (2018). New column simulations for the Viking landers: Winds, fog, frost, adsorption? *Icarus*, *310*, 48–53. https://doi.org/10.1016/j.icarus.2017.11.007

Schmidt, F., Douté, S., Schmitt, B., Vincendon, M., Bibring, J.-P., & Langevin, Y., & Omega Team. (2009). Albedo control of seasonal South Polar cap recession on Mars. *Icarus*, *200*(2), 374–394. https://doi.org/10.1016/j.icarus.2008.12.014

Schorghofer, N. (2020). Mars: Quantitative evaluation of crocus melting behind boulders. *The Astrophysical Journal*, *890*(1), 49. https://doi.org/10.3847/1538-4357/ab612f

Schorghofer, N., & Aharonson, O. (2005). Stability and exchange of subsurface ice on Mars. *Journal of Geophysical Research*, *110*(E5). https://doi.org/10.1029/2004JE002350

Schorghofer, N., & Edgett, K. S. (2006). Seasonal surface frost at low latitudes on Mars. *Icarus*, *180*(2), 321–334. https://doi.org/10.1016/j.icarus.2005.08.022

Schröder, S., Meslin, P.-Y., Gasnault, O., Maurice, S., Cousin, A., Wiens, R., et al. (2015). Hydrogen detection with ChemCam at Gale crater. *Icarus*, *249*, 43–61. https://doi.org/10.1016/j.icarus.2014.08.029

Singh, D., & Flanner, M. G. (2016). An improved carbon dioxide snow spectral albedo model: Application to Martian conditions. *Journal of Geophysical Research: Planets*, *121*(10), 2037–2054. https://doi.org/10.1002/2016je005040

Singh, D., Flanner, M. G., & Millour, E. (2018). Improvement of Mars surface snow albedo modeling in LMD Mars GCM with SNICAR. *Journal of Geophysical Research: Planets*, *123*(3), 780–791. https://doi.org/10.1002/2017JE005368

Smith, D., Neumann, G., Ford, P., Arvidson, R., Guinness, E. A., & Slavney, S. (1999). Mars global surveyor laser altimeter precision experiment data record [Dataset]. *NASA Planetary Data System, MGS-M-MOLA-3-PEDR-L1A-V1.0, 1999*. https://pds.nasa.gov/ds-view/pds/viewProfile.jsp?dsid=MGS-M-MOLA-5-MEGDR-L3-V1.0

Smith, I. B., & Spiga, A. (2018). Seasonal variability in winds in the north polar region of Mars. *Icarus*, *308*, 188–196. https://doi.org/10.1016/j.icarus.2017.10.005

Smith, M. D. (2002). The annual cycle of water vapor on Mars as observed by the Thermal Emission Spectrometer. *Journal of Geophysical Research*, *107*(E11), 25-1–25-19. https://doi.org/10.1029/2001JE001522

Smith, M. D. (2004). Interannual variability in TES atmospheric observations of Mars during 1999-2003. *Icarus*, *167*(1), 148–165. https://doi.org/10.1016/j.icarus.2003.09.010

Smith, P. H., Tamppari, L. K., Arvidson, R. E., Bass, D., Blaney, D., Boynton, W. V., et al. (2009). H_2O at the Phoenix landing site. *Science*, *325*(5936), 58–61. https://doi.org/10.1126/science.1172339

Spadaccia, S., Patty, C. H. L., Thomas, N., & Pommerol, A. (2023). Experimental study of frost detectability on planetary surfaces using multicolor photometry and polarimetry. *Icarus*, *396*, 115503. https://doi.org/10.1016/j.icarus.2023.115503

Spiga, A., & Smith, I. (2018). Katabatic jumps in the Martian northern polar regions. *Icarus*, *308*, 197–208. https://doi.org/10.1016/j.icarus.2017.10.021

Stcherbinine, A., Edwards, C. S., Smith, M. D., Wolff, M. J., Haberle, C., Al Tunaiji, E., et al. (2023). Diurnal and seasonal mapping of martian ices with emirs. *Geophysical Research Letters*, *50*(12), e2023GL103629. https://doi.org/10.1029/2023GL103629

Steele, L. J., Balme, M. R., Lewis, S. R., & Spiga, A. (2017). The water cycle and regolith–atmosphere interaction at Gale crater, Mars. *Icarus*, *289*, 56–79. https://doi.org/10.1016/j.icarus.2017.02.010

Svitek, T., & Murray, B. (1990). Winter frost at Viking Lander 2 site. *Journal of Geophysical Research*, *95*(B2), 1495–1510. https://doi.org/10.1029/jb095ib02p01495

Tamppari, L. K., & Lemmon, M. T. (2020). Near-surface atmospheric water vapor enhancement at the Mars Phoenix lander site. *Icarus*, *343*, 113624. https://doi.org/10.1016/j.icarus.2020.113624

Titus, T. N. (2005). Thermal infrared and visual observations of a water ice lag in the Mars southern summer. *Geophysical Research Letters*, *32*(24). https://doi.org/10.1029/2005GL024211

Titus, T. N., Kieffer, H. H., & Christensen, P. R. (2003). Exposed water ice discovered near the South Pole of Mars. *Science*, *299*(5609), 1048–1051. https://doi.org/10.1126/science.1080497

Valantinas, A., Thomas, N., Pommerol, A., Karatekin, O., Ruiz Lozano, L., Senel, C. B., et al. (2024). Evidence for transient morning water frost deposits on the Tharsis volcanoes of Mars. *Nature Geoscience*, *17*(7), 608–616. https://doi.org/10.1038/s41561-024-01457-7

Vignon, E., Genthon, C., Barral, H., Amory, C., Picard, G., Gallée, H., et al. (2016). Momentum- and heat-flux parametrization at Dome C, Antarctica: A sensitivity study. *Boundary-Layer Meteorology*, *162*(2), 341–367. https://doi.org/10.1007/s10546-016-0192-3

Vincendon, M. (2015). Identification of Mars gully activity types associated with ice composition. *Journal of Geophysical Research: Planets*, *120*(11), 1859–1879. https://doi.org/10.1002/2015je004909

Vincendon, M., Forget, F., & Mustard, J. (2010). Water ice at low to midlatitudes on Mars. *Journal of Geophysical Research (Planets)*, *115*(E10), E10001. https://doi.org/10.1029/2010JE003584

Vincendon, M., Massé, M., & Schmidt, F. (2014). Water ice, CO_2 ice, and active processes on Pole facing slopes. In LPI Editorial Board (Ed.), *Eighth international conference on Mars* (Vol. 1791, p. 1237).

Vincendon, M., Mustard, J., Forget, F., Kreslavsky, M., Spiga, A., Murchie, S., & Bibring, J.-P. (2010). Near-tropical subsurface ice on Mars. *Geophysical Research Letters*, *37*(1). https://doi.org/10.1029/2009gl041426

Wagstaff, K. L., Titus, T. N., Ivanov, A. B., Castaño, R., & Bandfield, J. L. (2008). Observations of the north polar water ice annulus on Mars using THEMIS and TES. *Planetary and Space Science*, *56*(2), 256–265. https://doi.org/10.1016/j.pss.2007.08.008

Williams, K., McKay, C. P., & Heldmann, J. (2015). Modeling the effects of Martian surface frost on ice table depth. *Icarus*, *261*, 58–65. https://doi.org/10.1016/j.icarus.2015.08.005

Williams, K. E., Toon, O. B., Heldmann, J. L., McKay, C., & Mellon, M. T. (2008). Stability of mid-latitude snowpacks on Mars. *Icarus*, *196*(2), 565–577. https://doi.org/10.1016/j.icarus.2008.03.017

Wilson, R. J., Lewis, S. R., Montabone, L., & Smith, M. D. (2008). Influence of water ice clouds on Martian tropical atmospheric temperatures. *Geophysical Research Letters*, *35*(7). https://doi.org/10.1029/2007GL032405

Wilson, R. J., Neumann, G. A., & Smith, M. D. (2007). Diurnal variation and radiative influence of Martian water ice clouds. *Geophysical Research Letters*, *34*(2). https://doi.org/10.1029/2006GL027976

Withers, P. (2012). Empirical estimates of Martian surface pressure in support of the landing of Mars science laboratory. *Space Science Reviews*, *170*(1–4), 837–860. https://doi.org/10.1007/s11214-012-9876-2

Yoldi, Z., Pommerol, A., Poch, O., & Thomas, N. (2021). Reflectance study of ice and Mars soil simulant associations – I. H_2O ice. *Icarus*, *358*, 114169. https://doi.org/10.1016/j.icarus.2020.114169

Zent, A. P., Hecht, M. H., Cobos, D. R., Wood, S. E., Hudson, T. L., Milkovich, S. M., et al. (2010). Initial results from the thermal and electrical conductivity probe (TECP) on Phoenix. *Journal of Geophysical Research*, *115*(E3). https://doi.org/10.1029/2009je003420

Zuber, M. T., Smith, D. E., Solomon, S. C., Muhleman, D. O., Head, J. W., Garvin, J. B., et al. (1992). The Mars Observer laser altimeter investigation. *Journal of Geophysical Research*, *97*(E5), 7781–7797. https://doi.org/10.1029/92JE00341